

WORTECS



Project-ID: 761329

WORTECS

Networking research beyond 5G

D4.5 - Optical Wireless Communications Proof-of-Concept

Contractual Date of Delivery:	2020, September 30th
Actual Date of Delivery:	2020, October 28th
Editor(s):	Dominic O'Brien (UOXF)
Author(s):	Ravinder Singh, James Farmer, Grahame Faulkner (UOXF), Bastien Béchadergue (Oledcomm), Rui Bian, Tamas Weszely (pureLiFi), Rafael Pérez, Víctor Guerra, José Rabadan (ULP), Guillaume Vercasson, Rodolphe Legouable (B<>COM), Brzozowski Marcin, Sark Vladica (IHP), Olivier Bouchet (Orange), Marc Lanoiselée (B<>COM)
Work package:	WP4
Security:	PU
Nature:	Deliverable
Version:	version 1.0
Total number of pages:	65

Abstract

This deliverable in project WORTECS presents Proof-of-Concepts (PoCs) for indoor Optical Wireless Communication (OWC) systems using broad and narrow optical beams. The broad optical beam OWC PoC aims to provide Gbit/s links to multiple users without the need for localisation and beam steering. Whereas the narrow beam OWC PoC, here referred to as fiber-wireless-fiber (FWF) PoC, aims for beyond Tbit/s links using tracking and beam-steering. These PoCs are tested in a real-world application scenario where virtual reality (VR) content is delivered from a video server to VR head mounted displays (HMDs) through the PoC air interfaces. The different OWC links are managed by heterogeneous network (HetNet) architecture implemented on FPGAs. The link reliability is tested through evaluation of bit error ratio (BER), achievable throughput, receiver sensitivity and coverage. The propagation model for the OWC PoCs are also presented.

Oledcomm (OLD), B<>COM (BCM) and pureLiFi (PLF) develop the Gbit/s OWC PoCs. The FWF PoC is developed by the University of Oxford (UOXF). The PoCs are managed by HetNet board programmed by IHP. Virtual Reality (VR) or Mixed Reality (MR) use case is shown with the help of Video Converter (VC) board and Virtual Reality content from BCM. Propagation model first results are presented by the University of Las Palmas (ULP).

Keyword list

Optical wireless transmission, Fibre Wireless Fibre (FWF), FiWi (Fibre Wireless), Heterogeneous Networks (HetNet), Throughput, Coverage, Virtual Reality

List of Authors

First name	Last name	Beneficiary	Email address
Ravinder	Singh	UOXF	ravinder.singh@eng.ox.ac.uk
Dominic	O'Brien	UOXF	dominic.obrien@eng.ox.ac.uk
James	Farmer	UOXF	james.farmer2@balliol.ox.ac.uk
Grahame	Faulkner	UOXF	grahame.faulkner@eng.ox.ac.uk
Rui	Bian	pureLiFi	rui.bian@purelifi.com
Tamas	Weszely	pureLiFi	tamas.weszely@purelifi.com
Bastien	Béchadergue	OLD	bastien.bechadergue@oledcomm.net
Rafael	Pérez	ULPGC	rperez@dsc.ulpgc.es
Víctor	Jiménez	ULPGC	victor.guerra@fpct.ulpgc.es
Guillaume	Guerra	ULPGC	victor.guerra@fpct.ulpgc.es
Guillaume	Yáñez	ULPGC	victor.guerra@fpct.ulpgc.es
Guillaume	Vercasson	b<>com	guillaume.vercasson@b-com.com
Marcin	Brzozowski	IHP	brzozowski@ihp-microelectronics.com
Vladica	Sark	IHP	sark@ihp-microelectronics.com
Rodolphe	Legouable	b<>com	Rodolphe.legouable@b-com.com
Olivier	Bouchet	ORANGE	olivier.bouchet@orange.com
Marc	Lanoiselée	b<>com	marc.lanoiselee@orange.com

Document History

First name	Last name	Version	Comments
Ravinder	Singh	13 May 2020	ToC, and edited FWF demonstrator description, and edited FWF demo-I experimental results
Rui	Bian	30 Aug 2020	Section II editing
Guillaume	Vercasson	07 Sep 2020	Section III editing
Victor	Guerra	22 Sep 2020	Section V editing
Ravinder	Singh	20 Sep 2020	Updated Section 4 on FWF PoC and combined inputs from BCOM, PLF and ULP
Guillaume	Vercasson	28 Sep 2020	Section III finalised
Rui	Bian	24 Sep 2020	Finalised Section III
Bastien	Béchadergue	30 Sep 2020	Edited Section III
Ravinder	Singh	07 Oct 2020	Combined inputs from BCOM, PLF and OLD. Prepared new draft.
Dominic	O'Brien	08 Oct 2020	Review and Editing

List of Acronyms

Acronym	Meaning
ACO-OFDM	Asymmetrically Clipped Optical OFDM
ADC	Analog to Digital Converter
A/D	Analog to Digital
AFE	Analog Front End
APD	Avalanche Photodiode
ASIC	Application-Specific Integrated Circuit
AWG	Additive White Gaussian
AWGN	Additive White Gaussian Noise
BER	Bit Error Rate
BLER	Bloc Error Rate
BP	Believe Propagation
CP	Cyclic Prefix
CIR	Channel Impulse Response
CFO	Carrier Frequency Offset
dB	Decibel
D/A	Digital to Analog
DAC	Digital-to-Analog Converter
DC	Direct Current
DCO-OFDM	DC biased Optical OFDM
DFT	Discrete Fourier Transform
DVB	Digital Video Broadcasting
EIRP	Effective Isotropic Radiated Power
FEC	Forward Error Code
FFC	Free-From Optical Concentrator
FFT	Fast Fourier Transform
FIR	Finite Impulse Response
FiWi	Fibre Wireless
FBMC	Filter-Bank Multicarrier
FOV	Field of View
FPGA	Field Programmable Gate Array
FWF	Fiber Wireless Fiber
FWHM	Full Width at Half Maximum
Gbps	Giga bits per second
GND	Ground
GUI	Graphical User Interface
HMD	Head Mounted Display
HSPA	High Speed Packet Access
IFFT	Inverse Fast Fourier Transform
IM/DD	Intensity Modulation / Direct Detection
IR	Infra-Red
ISI	Inter Symbol Interference
LDPC	Low Density Parity Check
LED	Light-Emitting Diode
LO	Local Oscillator
LOS	Line Of Sight

LTE	Long Term Evolution
MAC	Medium Access Control
MCRT	Monte Carlo Ray Tracing
MCS	Modulation and Coding Scheme
MIMO	Multiple-Input Multiple-Output
NIR	Near Infra-Red
NLOS	Non Line Of Sight
OFDM	Orthogonal Frequency Division Multiplex
OFDM-MConst	OFDM with multiple constellations
OFE	Optical Front End
OOB	Out Of the Band
O-OFDM	Optical OFDM
ODH	Optical Detector Head
OTH	Optical Transmission Head
OWC	Optical Wireless Communication
PA	Power Amplifier
PAM- DMT	Pulse-Amplitude-Modulated Discrete-Multitone
PAPR	Peak-to-Average Power Ratio
PCB	Printed Circuit Board
PCC	Parabolic Compound Concentrator
PHy	Physical layer
PRBS	Pseudo-Random Binary Sequence
P/S	Parallel to Serial
QC-LDPC	Quasi-Cyclic LDPC
RF	Radio Frequency
RMS	Root Mean Square
SC	Single Carrier or Successive-Cancellation
SCL	Successive-Cancellation List
SISO	Single Input Single Output
SNR	Signal to Noise Ratio
S/P	Serial to Parallel
SP	Sum-Product
SPI	Serial Peripheral Interface
TIR	Total Internal Reflections
UFMC	Universal Filtered Multi-Carrier
VC	Video Converter
VGA	Variable Gain Amplifier
VR	Virtual Reality
WORTECS	Wireless Optical/Radio Tera-bit CommunicationS
ZP	Zero Prefix

Table of contents

1	Introduction.....	10
2	Optical Wireless Communication PoC.....	12
2.1	Features.....	12
2.1.1	Digital board	12
2.1.2	Optic and Analog Board	13
2.2	Test Results.....	14
2.2.1	Digital Board Test	14
2.2.1	OFE Bandwidth Characterization.....	17
3	Hybrid RF and Optical Wireless Communication PoC.....	19
3.1	Features.....	19
3.1.1	System Overview.....	19
3.1.2	Digital board	21
3.1.2.1	FPGA connections	23
3.1.2.2	Power supply.....	24
3.1.2.3	Clock tree.....	24
3.1.3	Analog board.....	25
3.1.3.1	RF board.....	26
3.1.3.2	Radio board hardware	29
3.1.4	28GHz board.....	30
3.1.5	60GHz board.....	30
3.1.6	Optoelectronic board.....	30
3.2	Theoretical link budget.....	34
3.2.1	Optical link budget.....	34
3.2.2	LDPC performance.....	35
3.2.3	OFDM frame structure	36
3.2.4	System throughput	36
3.3	Test results.....	37
3.3.1	GUI.....	37
3.3.1.1	Low level control	37
3.3.1.2	System control	38
3.3.1.3	Monitoring.....	39
3.3.2	Digital section.....	40
3.3.3	60GHz section.....	42
3.3.4	Hybrid full duplex transmission.....	43
4	Fibre Wireless Fiber PoC.....	44
4.1	Features.....	44
4.1.1	System Description	44
4.1.2	Terminal Control	46
4.2	Characterisation of Localisation System: FoV, Link-Loss, Aberrations and Latency.....	48
4.2.1	System Setup.....	48
4.2.2	Field of View (FoV).....	48
4.2.3	Aberrations and Calibration	49
4.2.4	Tracking Latency Evaluation.....	50
4.3	Terabit/s FWF Transmission Results	50
4.4	Real-time Transmission of VR Content.....	53
5	Propagation Model.....	58
5.1	High level simulation model.....	58
5.2	Mathematical description of the simulation model.....	59

5.3	Design of the Software as a Service platform	60
6	Conclusions	63
7	References	64

List of Tables

Table 1: OWC PoC digital board specifications.....	12
Table 2: OWC PoC OFE specifications.....	13
Table 3: Dependence between the channel bandwidth and the SNR to reach 850 Mbps and 1 Gbps respectively, with the G.hn baseband.....	17
Table 4: Measured -3dB bandwidth of the OFE transmitter and receiver.....	18
Table 5: Digital board main components.....	22
Table 6: Tx theoretical results.....	34
Table 7: Rx theoretical results.....	34
Table 8: OFDM physical layer parameters.....	36
Table 9: Estimated output throughput for a single optical link.....	37
Table 10: Supported feature of the digital section.....	40
Table 11: FWF Demonstrator Notation and Parameters.....	45
Table 12: System features and specification.....	50
Table 13: Parameters of WORTECS Saas API endpoint.....	61

List of Figures

Figure 1: WORTECS PoC Demonstrator-V2.....	10
Figure 2: Digital board overview.....	12
Figure 3: Optical front-end overview.....	13
Figure 4: A snapshot of the Spirit Config Tool software for the board configuration.....	14
Figure 5: An example of the measured SNR in one direction.....	15
Figure 6: Digital board - iperf server with 948 Mbps measured data rate.....	16
Figure 7: Digital board - iperf server with 947 Mbps measured data rate.....	16
Figure 8: View of the G.hn baseband board with optimized form factor.....	17
Figure 9: View of the OFE (top board, case of a PIN photodiode and VCSEL) connected to the G.hn baseband board (bottom).....	18
Figure 10: Platform overview.....	19
Figure 11: Multi-RAT Platform capabilities.....	20
Figure 12: Analog and digital part of the platform schematic.....	21
Figure 13: Digital board front view.....	23
Figure 14: Digital board rear view.....	23
Figure 15: Multi-RAT platform clock tree.....	25
Figure 16: Tx schematic of the RF board.....	26
Figure 17: Rx schematic of the RF board.....	27
Figure 18: Base band and radio signal example.....	27
Figure 19: Base band and radio signal example.....	28
Figure 20: Analog RF board front view.....	29
Figure 21: Analog RF board rear view.....	30
Figure 22 : Optical Tx and Rx mezzanine boards / main advantages.....	31
Figure 23 : 850 nm Tx diffracted laser diode.....	31
Figure 24 : Tx laser diodes driving mode.....	32
Figure 25 : Tx laser conventional driver / diffracted characteristics.....	32
Figure 26 : Tx laser low power consumption driver used mode.....	33
Figure 27 : Rx Avalanche Photo Diode.....	33
Figure 28 : Rx preamplifier synoptic.....	34
Figure 29: LDPC performances vs SNR, for 1 or 2 iteration, from BPSK to 256QAM.....	35
Figure 30: LDPC decoding architecture.....	36
Figure 31: OFDM control GUI : OFDM Tab.....	38
Figure 32: System control GUI.....	38
Figure 33: Monitoring GUI : received samples view.....	39
Figure 34: Monitoring GUI : de-mapping view (256QAM).....	40
Figure 35: OFDM control GUI : ADC samples view (prefect channel).....	41
Figure 36: OFDM control GUI : channel estimation view.....	41
Figure 37: OFDM control GUI : de-mapping view with base band transmission.....	41
Figure 38: Modem with 60GHz patch antenna and focussing lens.....	42
Figure 39: 60GHz patch antenna and focussing lens.....	42
Figure 40: Two modem with 60GHz downlink and base band uplink.....	43
Figure 41: 60GHz receiver performances.....	43
Figure 43: Block diagram of FWF system.....	44



Figure 44: Additional loss (dB) due to pointing misalignment. Left hand figure shows transmitter pointing, receiver static. Right hand figure shows receiver pointing, transmitter static. 45

Figure 45: Assembled receiver (left) and transmitter (right) units. 46

Figure 46: The IR beacon as seen by coarse (left) and fine (right) tracking cameras at 3 meter distance. 46

Figure 47: Localisation and steering process for terminal alignment. 47

Figure 48: Experimental setup for FoV and aberration evaluation. 48

Figure 49: Link-loss (dB) vs link-angle for the two FWF terminals. The solid curves represent received power without aberration corrections and the dashed curves with aberration correction. 48

Figure 50: Steering angle correction (Degree) for one of the terminals for steering in horizontal plane (left) and vertical plane (right). 49

Figure 51: The time versus received power plot for the manual translation of the Terminal-B in lateral direction with respect to Terminal-A. The inset shows time versus link angle for the Terminal-B, to study the terminal tracking latency. 49

Figure 52: Experimental layout for testing 1 Tbit/s transmission over the FWF terminals. 51

Figure 53: Experimental setup for testing 1 Tbit/s transmission over the FWF terminals. 51

Figure 54: The transmitted and received optical spectra of the 10 WDM channels (left), measured BER curves versus received optical power (ROP) for all WDM channels (right) for optimal alignment at location L1. 52

Figure 55: At the four discrete locations, for both OWC links established by the tracking system and manually optimized OWC links, (left) BER curves of all WDM channels at -10 dBm received optical power, and (right) corresponding optical link loss. 52

Figure 56: BER curves (left) of all the WDM channels at location L1 and location L4 for both tracking established OWC links and manually optimized OWC links at -10 dBm received optical power. A typical 100 Gb/s PAM-4 eye diagram (Right) at -9 dBm ROP for the manually optimised OWC link at location 1. 53

Figure 57: BER performance of FTLX1871M3BCL SFP+ module for a 10.3 Gbit/s free-space transmission. 54

Figure 58: Bore sight communication range of FWF terminals with SFP+ based 10.3 Gbit/s free-space transmission. 54

Figure 59: FWF terminal setup in 4 x 4 x 3 meter indoor testing facility at BCOM laboratory. The AP terminal in one corner at 3.5m height (left), the UE terminal on the room floor (centre) and VR-HMD connected to the UE terminal (right). 55

Figure 60: FWF terminal down-link (top) and up-link (bottom) received power levels (dBm) for 10.3 Gbit/s free-space transmission when the UE terminal moved across the room floor. 56

Figure 61: Experimental setup for data transmission using VR content. 56

Figure 62: WORTECS Software as a Service architecture. 61

Figure 63: Web interface for WORTECS SaaS. 62

1 Introduction

This deliverable focuses on Proof-of-Concept (PoC) communication systems based on optical wireless communications for multi-Gigabit per second and beyond wireless transmission. The main objective is to present the features of the developed PoCs and discuss the test results in terms of throughput, latency, positioning, capacity and coverage. These PoCs are expected to be used in a Heterogeneous Network (HetNet) architecture, for cooperation or aggregation between different Wireless Access Technologies (WAT) providing seamless user connectivity.

This deliverable is divided into several parts. Each parts containing specific PoC, and describes the main features followed by characterisation and test results. Figure 1 shows the global setup of the WORTECS PoC demonstrators, with the different prototypes integrated for virtual reality (VR) application. Seven PoCs have been developed to meet project proposal objectives, i.e. achieve Terabit per second (Tbit/s) by using radio or optical wireless communication links with an ultra-fast heterogeneous network management device. The three PoCs concerned within this deliverable are PoC 3, the Optical Wireless Communications (OWC) devices; PoC 6, the Fiber Wireless Fiber (FWF/FiWi) system and PoC 7, the hybrid radio and optic solution (OWC/60GHz).

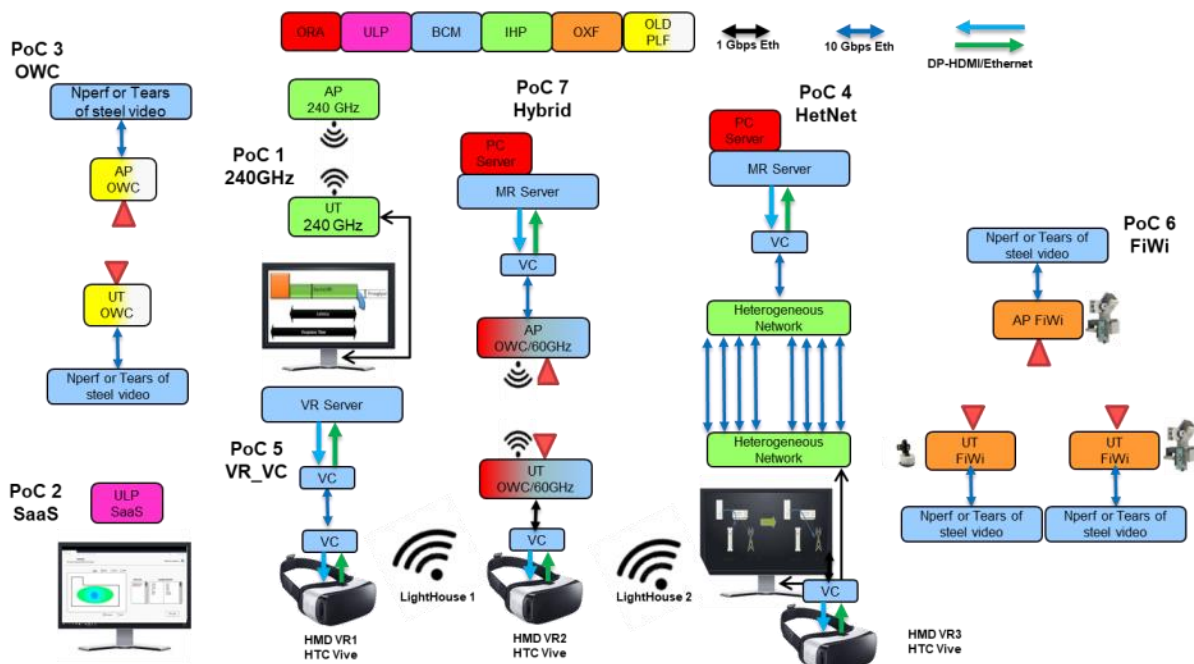


Figure 1: WORTECS PoC Demonstrator-V2.

The OWC PoC (or the PoC 3), has been developed by PLF and OLD partners. The aim here is Gbps capability for each user within an indoor environment. The indoor access network setup in this case is expected to use multiple broad-beam optical links for sufficient coverage and user mobility. The broad beam OWC setup relaxes the tracking requirements by trading the achievable capacity. This deliverable describes the design of the digital and analog front-end boards developed for the OWC PoC along with relevant specifications obtained through some preliminary experiments. Following this, the deliverable presents the hybrid RF and optical system PoC (PoC 7), developed by the BCM partner as part of a multi-RAT approach explored for the transceiver design within the WORTECS project. The focus of the PoC 7 has been on the development of the digital and analog front-end boards that are capable of working with different radio and optical air-interfaces. A detailed description of the design of the digital and analog boards is provided and some initial test results are discussed.

The deliverable also presents the FWF PoC (PoC 6), which has been developed by UOXF partner within the WORTECS project. The aim of the FWF PoC is ultra-high data rate capability and delivery of Tbps capacities to individual or multiple users. This is achieved using steerable narrow-beam optical links with support from a high accuracy, low latency localisation and tracking system. This PoC uses commercial off-the-shelf beam steering mirrors, fibre collimators, fibre pigtailed sources and detectors for the Tbps capable communication links. Small form factor, cost effective component use is targeted for the design of the localisation system. Overall, a compact design of beam delivery terminals is achieved, while ensuring that practical coverage in an indoor environment is achieved.

In the end, the deliverable presents channel simulation tool developed by the ULP partner. Here, the design of a wireless propagation model for the 60 GHz and beyond RF, and optical electromagnetic waves is discussed. A high level channel simulation model along with a detailed mathematical description is presented. The design of a software as a service platform is also presented.

2 Optical Wireless Communication PoC

This section presents the OWC PoC for Gbps links developed within the WORTECS project. The details of the digital baseband processing board and the optical front-end are discussed and some preliminary results are presented which show the Gbps capability of the OWC PoC.

2.1 Features

2.1.1 Digital board

The developed digital board is based on the ITU-T G.hn standard [1]. The top-level schematic of the developed digital board is shown in Figure 2. The Ethernet interface shall be a 1000 Mbps interface. The Gbps baseband module features a MaxLinear wave-2 G.hn digital baseband processor [2]. The analog front end module features a MaxLinear wave-2 G.hn AFE with a single transmission and reception channel to enable SISO 200 MHz operation [3]. It offers:

- Programmable transmission and reception gains
- Integrated filters
- Integrated line drivers
- Equalization in reception
- Very low noise and distortion over the entire transmission and reception paths

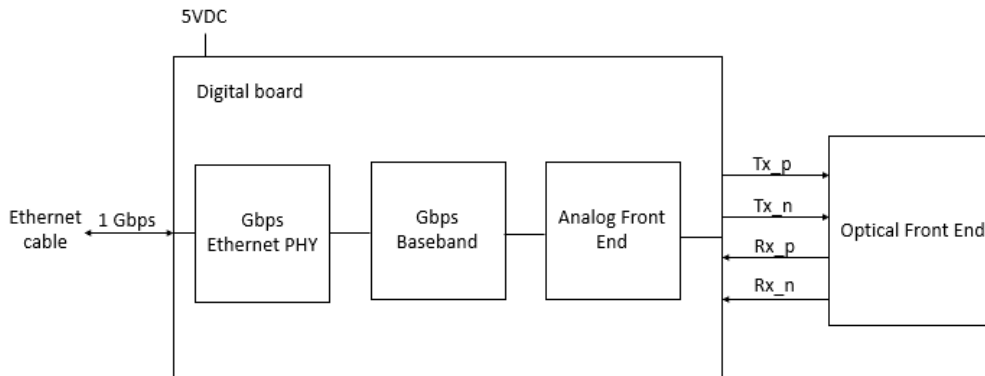


Figure 2: Digital board overview.

Table 1: OWC PoC digital board specifications

Parameter	Value	Unit
Supply Voltage	5 (4.75 to 5.25)	VDC
Supply Current	1	A
Data Interface	Gigabit Ethernet Port	-
Throughput Rate	956	Mbps
Interface with OFE	Choice of board to board or via cable harness	-
Temp Range	0 to 40	°C

The PoC digital board specifications are presented in Table 1. The typical operation supply voltage is 5 V while a current of 1 A is required for the digital board without the OFE. Thus, the OFE current needs to be added for the power supply

unit requirement. The data interface is implemented with a Gigabit Ethernet port. The maximum throughput rate of the digital board is 956 Mbps, which is the maximum Ethernet throughput on a Gigabit Ethernet link. On the interface with OFE, it could be implemented as either board to board connection or via cable harness. The performance evaluation tests on the digital board are discussed in Section 2.2.1.

2.1.2 Optic and Analog Board

The analog front-end (AFE) included in the digital baseband previously described is connected to an optical front-end. The role of the AFE is to convert the analog data signal to transmit into an optical signal and conversely to convert the optical data signal received into an analog electrical signal that is conveyed to the baseband for further processing. The high-level architecture of the OFE is shown in Figure 3.

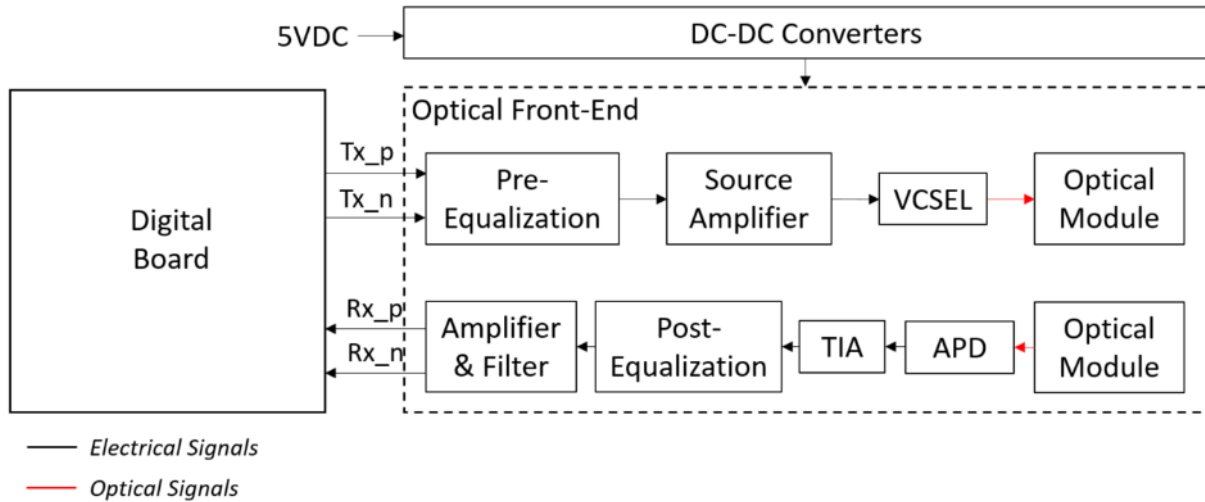


Figure 3: Optical front-end overview.

On the transmitting path, the AFE is composed of a pre-equalization stage followed by source amplifier to format the input differential analog signal (Tx_p and Tx_n) into a DC+AC signal suitable to drive the light source. This light source here is a VCSEL (OSRAM PLPVQ 940A) with greater than 400 MHz bandwidth, which already integrates a diffuser to ensure non-coherent light emission. This VCSEL may be used in with a custom-made optical module used to reshape and focus its light beam pattern. On the receiving path, an optical module, more precisely an optical concentrator, is used to focus the incoming light beam toward a photoreceiver. Two sorts of photoreceivers could be used: PIN photodiodes and avalanche photodiodes (APD). PIN photodiodes usually have larger sensitive area than APD, they do not need to be biased with high voltage (< 50V) and they are usually rather cheap. On the other hand, properly biased APDs (usually > 150V) usually have a photosensitivity that can be a hundred times larger than that of PIN photodiodes. However, they also usually have small areas and larger prices than PIN photodiodes. Given their respective advantages – mainly technical for APD and economical for PIN – both kinds of receivers are investigated with the objective to eventually fulfill the data rate specifications for VR content transmission. The PIN photodiode considered is a Hamamatsu S6968, which comes with an integrated optical concentrator. On the other hand, the APD considered is a Hamamatsu S8890-15, on which a custom-made concentrator is added. In both cases, a trans-impedance amplifier (TIA) is then used to convert the photocurrent into a voltage signal that is then processed via post-equalization, filtering and amplification analog stages. **Erreur ! Source du renvoi introuvable.** presents the main characteristics of the OFE.

Table 2: OWC PoC OFE specifications.

Power Supply and Interface Parameters	
Parameter	Value
Supply voltage	5 V
Supply current	320 mA (in full duplex)

Power supply interface	USB-C
Baseband interface	Board-to-board PCB connector
Transmitter Parameters	
Parameter	Value
Transmitted optical power range	135 mW +/- 55 mW
Full angle at half power (without optical module)	65° (horizontal) x 78° (vertical)
Wavelength of operation	940 nm
Receiver Parameters (APD case)	
Parameter	Value
Optical gain	Not tested at present
Sensitive area	1.77 mm ²
Photosensitivity (at 940 nm)	50 A/W
Full angle at half sensitivity	120°
Receiver Parameters (PIN photodiode case)	
Parameter	Value
Optical gain	Included in sensitive area
Sensitive area	150 mm ² (includes optical gain)
Photosensitivity (at 940 nm)	0.67 A/W
Full angle at half sensitivity	70°

Note that the transmitted optical power can be easily modified at the OFE level in order to be adapted to potential changes in the admissible limit of emission (AEL) that could occur when focusing the transmitter light beam. Here the value 135 mW +/- 55 mW corresponds to the DC level +/- the OFDM swing, and has been calculated to respect the class 1 AEL for the VCSEL source without additional optical module (i.e. with emission angle as given in Table 2).

In this section, tests of both the digital board and the OFE are detailed. The tests and performance of the assembly will be provided in deliverable 4.7.

2.2 Test Results

2.2.1 Digital Board Test

Initial tests were performed on the implemented digital boards for the performance evaluation without the use of OFE (See Figure 6 and Figure 7 for setup.). The target was to investigate the performance of the G.hn based connection itself. Thus, the two digital boards were directly connected using four cables for the two (transmission and reception) differential signal pairs. Note that four additional 6 dB attenuators were used in the four links. Then each digital board was connected to a laptop via Ethernet cable. G.hn based connection is established between both digital boards automatically after powering on. The devices could be configured using Spirit Config Tool software as shown in Figure 4.

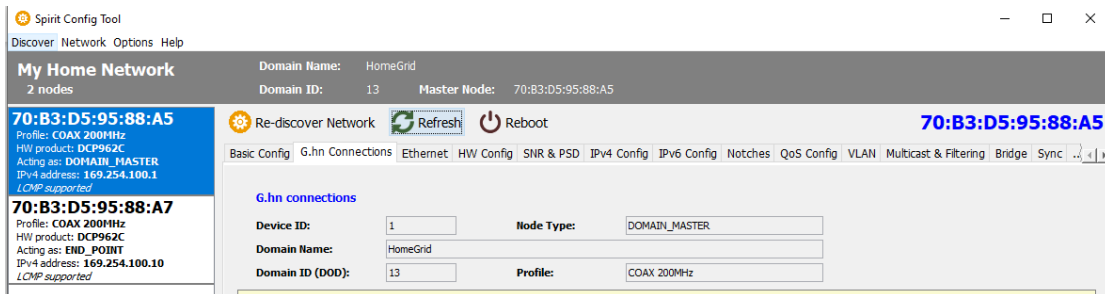


Figure 4: A snapshot of the Spirit Config Tool software for the board configuration.

With the four 6 dB attenuators connected and setting the transmitter gain to 4, the digital boards would be able to offer the ~1 Gbps link as expected. Figure 5 shows an example of the measured signal-to-noise ratio (SNR) in one direction. With this setting, approximately flat SNR curve within 200 MHz could be achieved with an average SNR of over 36 dB.

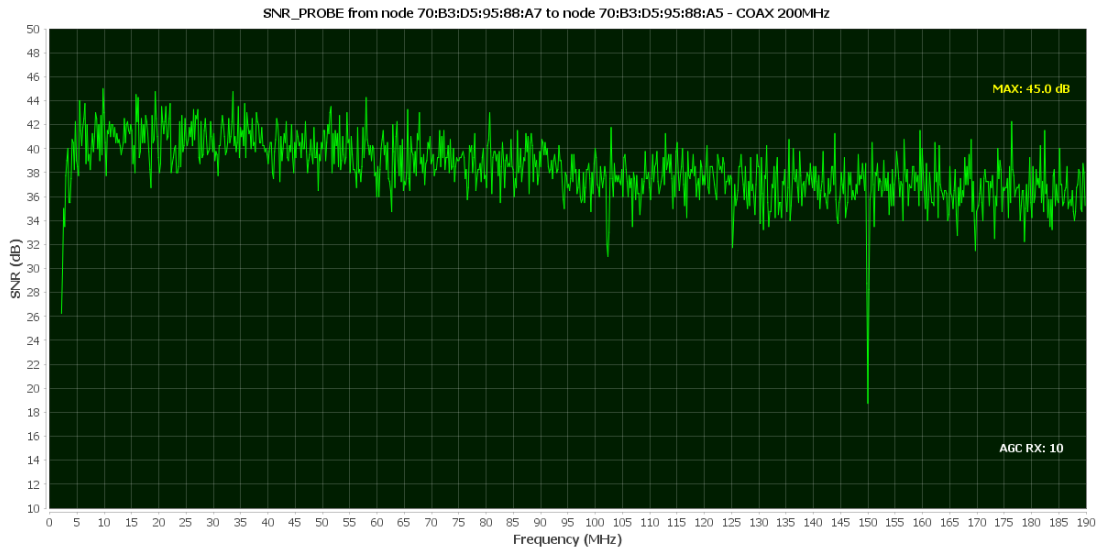


Figure 5: An example of the measured SNR in one direction.

A data rate measurement was then performed with the use of *iperf3* function. One laptop was set up as the *iperf3* server while another laptop being set up as the client. Bidirectional data transfer was established between the server and the client through the G.hn connection between the digital boards. Figure 6 shows the digital board what has been set up as the server. Continuous measurement was taken and it can be seen that ~948 Mbps throughput was achieved. On the other direction, as shown in Figure 7, similar throughput was achieved. As explained in the previous section, this throughput is limited by the Gigabit Ethernet link. With these settings being used, the results have shown that the implemented digital boards are capable of delivering a bidirectional link with the expected throughput.

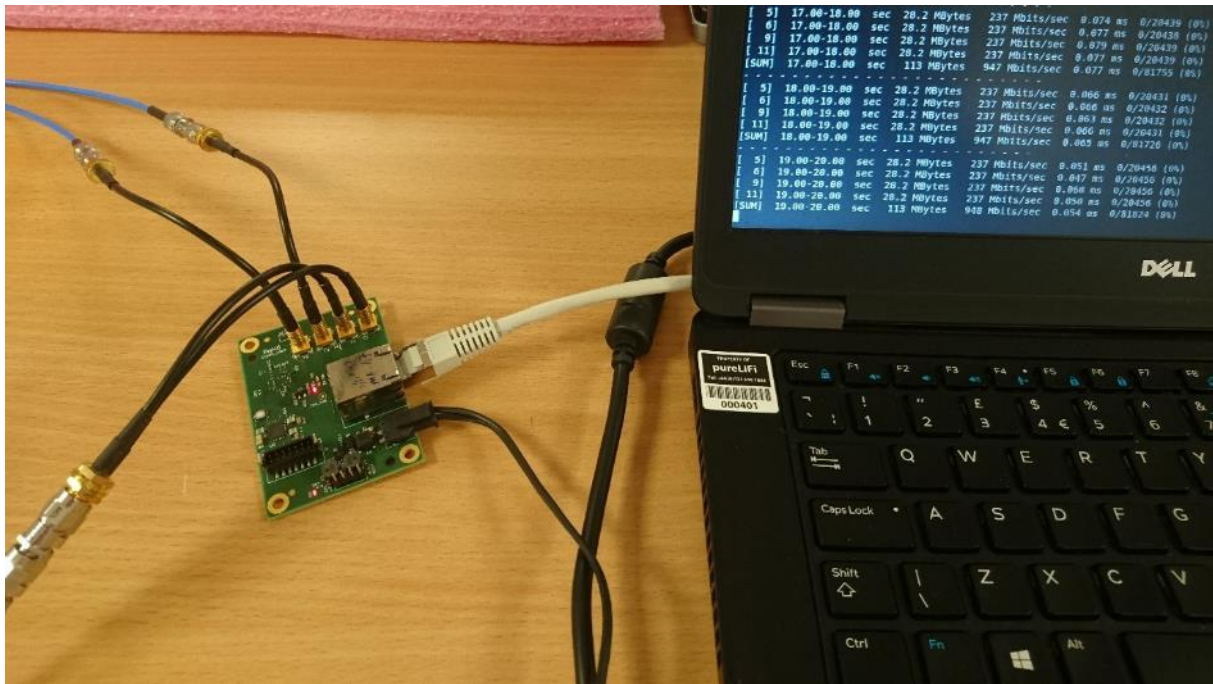


Figure 6: Digital board - iperf server with 948 Mbps measured data rate.

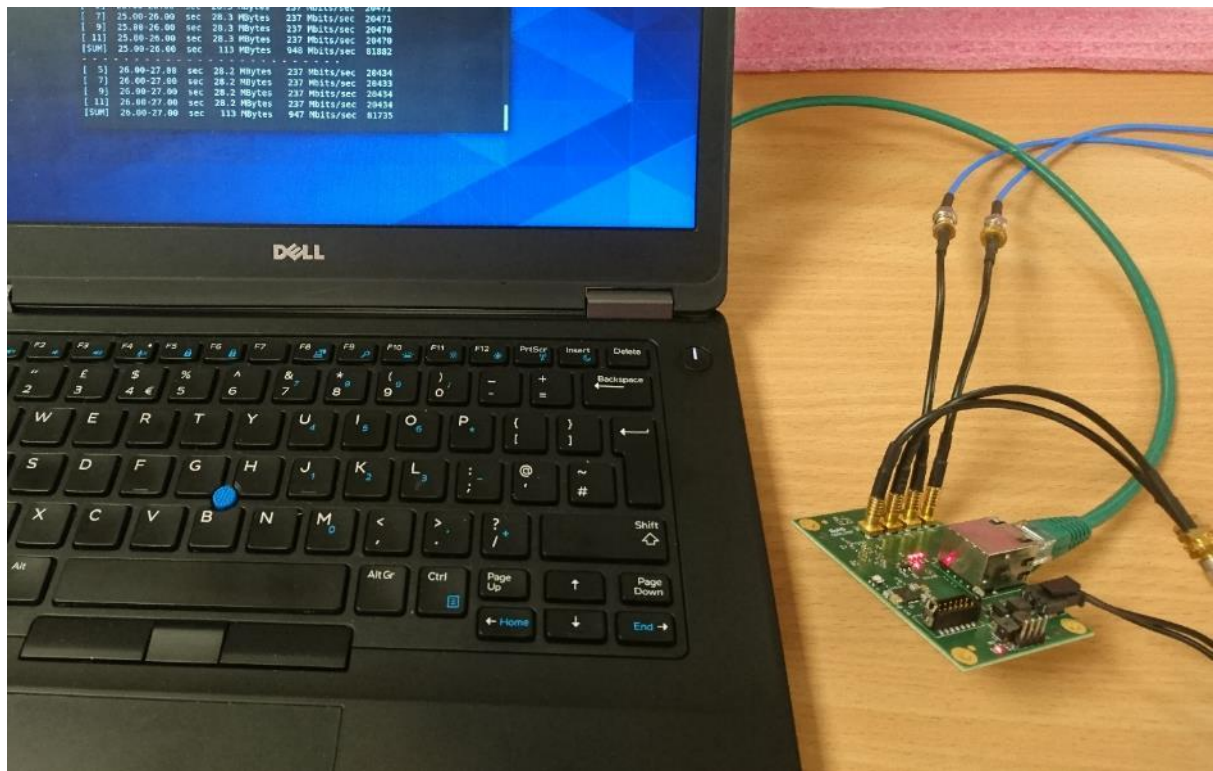


Figure 7: Digital board - iperf server with 947 Mbps measured data rate.

In parallel, a similar G.hn baseband board has been designed by Oledcomm (OLD) with a different form factor (55 mm diameter) to ease interconnection with the OFE, as represented in Figure 8.

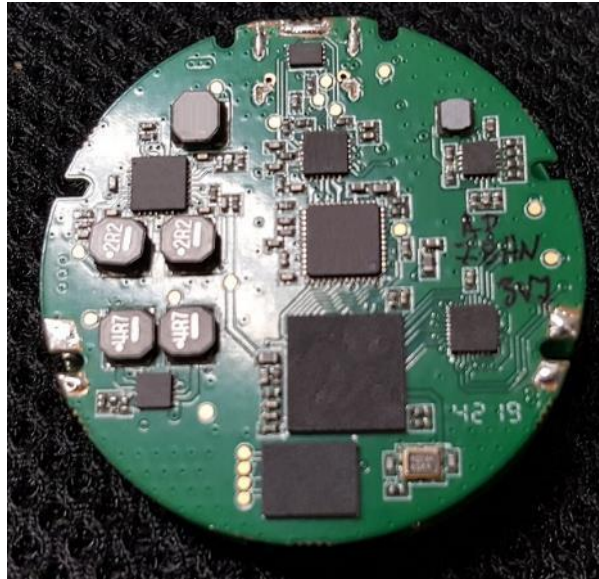


Figure 8: View of the G.hn baseband board with optimized form factor.

This board has also been tested with both the Spirit Config Tool and the *iperf3* tool and can reach data rates up to around 1 Gbps. The data rate depends obviously on the SNR. Table 3: Dependence between the channel bandwidth and the SNR to reach 850 Mbps and 1 Gbps respectively, with the G.hn baseband. Table 3 shows, for a given ideal channel bandwidth, the SNR required to reach 850 Mbps and 1 Gbps.

Table 3: Dependence between the channel bandwidth and the SNR to reach 850 Mbps and 1 Gbps respectively, with the G.hn baseband.

Channel bandwidth	SNR to get 850 Mbps	SNR to get 1 Gbps
100 MHz	45 dB	Not reachable
150 MHz	31 dB	35 dB
200 MHz	23 dB	28 dB

2.2.1 OFE Bandwidth Characterization

The baseband board shown on Figure 8 can be connected to the OFE shown in Figure 9. The version represented in this figure is using a VCSEL as light source and the PIN photodiode as photoreceiver. However, as previously mentioned, the OFE has been designed to operate also with an APD as photoreceiver, in which case an additional board has been designed and can be connected to the OFE to provide enough bias voltage to the APD.

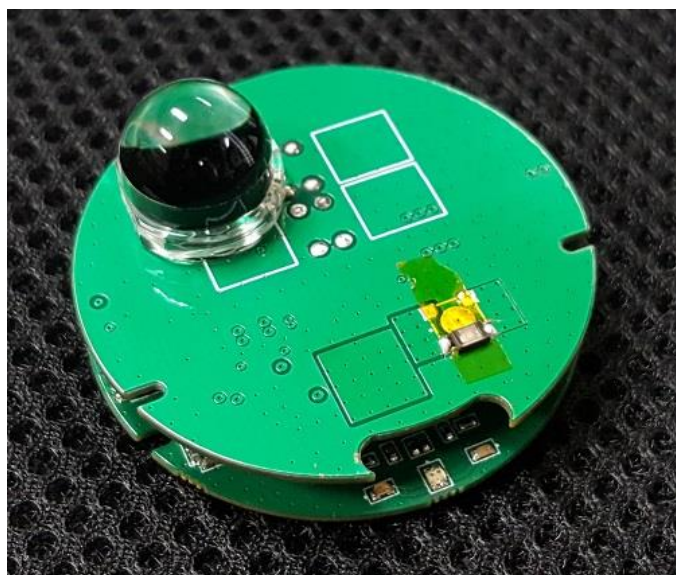


Figure 9: View of the OFE (top board, case of a PIN photodiode and VCSEL) connected to the G.hn baseband board (bottom).

Table 4 shows the -3 dB bandwidth measurement results for the transmitter as well as both receivers (PIN photodiode and APD). Note that these bandwidth are -3 dB bandwidth, which means we can expect better performance than those announced in Table 3, where the channel bandwidth is given at -40dB. In any case, we cannot expect to reach 1 Gbps with the PIN photodiode because of its limited bandwidth but should still be able to achieve approximately 850 Mbps. With an APD, on the other hand, a data rate of 1 Gbps should be reachable. Detailed test and performance results, including data rate, PER and latency spatial distribution according to the communication distance will be available in Deliverable D4.7.

Table 4: Measured -3dB bandwidth of the OFE transmitter and receiver.

-3 dB Bandwidth Measured	
Transmitter (with VCSEL)	200 MHz
Receiver (with PIN photodiode)	100 MHz
Receiver (with APD)	170 MHz

3 Hybrid RF and Optical Wireless Communication PoC

This section details the PoC 7 (see Figure 1), a hybrid RF and optical wireless communication, developed by BCOM within this project. The digital and analog boards described here have multi-RAT capability and could work with different RF and optical front-end systems.

3.1 Features

3.1.1 System Overview

The hardware platform planned for the prototype realization is shown in Figure 10, from left to right, digital board, with RF board and with final cover. It is a compact size equipment, A5 format, consisting of the combination of two main boards: a very high data rates digital one, highly programmable and based on FPGAs, and a second for the processing of the very broadband radio frequency analog signals, comprising two sets of radio transmitter / receiver.

Additionally, to enlarge the wireless capabilities of the system, daughter boards can be plugged onto the RF board. Three set of them can be used:

- One to address 28GHz Radio frequencies
- One to address 60GHz Radio frequencies
- One to address optical communication using IR wave length

Figure 10 shows, from left to right, the digital board side view, then the radio frequency board side view with the antennas, and finally, the two plugged boards set all in a box.

As can be seen, the boards are arranged vertically so as to accommodate the various constraints of:

- connectivity
- heat dissipation
- radio board antenna positioning



Figure 10: Platform overview.

The combination of these two complementary boards thus makes it possible to constitute a hardware platform of multi-RAT capabilities, with various radio transmission modes, in MIMO 2x2, or more, and for very wide operating frequency bands applications, including the millimeter waves band of 28GHz, 60 GHz or even an optical front end (these boards does not appear in this picture), as specified in Figure 11.

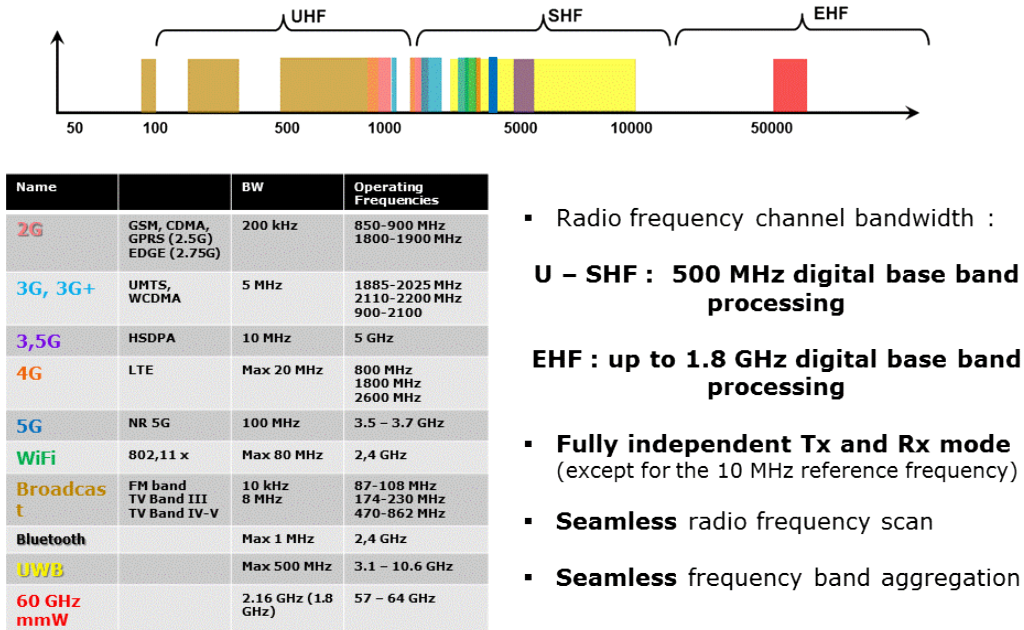


Figure 11: Multi-RAT Platform capabilities.

A block diagram of the platform is presented in Figure 12, with the digital part in the blue background, and the RF analog part in the green one.

The digital board (which deals with the digital part) is able to generate or acquire complex baseband analog signals (I and Q channels) up to 800 MHz bandwidth.. It deals with the bit level information, as OFDM modulation, LDPC code correction, or high speed optical interfaces. It can be used in standalone mode or associated with an analog board thanks to dedicated high speed connectors (HSMC family).

The analog board (named the RF board) deals with conditioning the signals for the daughter board. It can add some filtering, some frequency transposition and deals with the generation of a clean frequency reference.

Finally, daughter boards can generate/receive signals including 28GHz, 60GHz or optical (850nm/950nm) signal, depending of the one that has been selected. The 60GHz board is described in 3.1.5, and the optical board is described in 3.1.6.

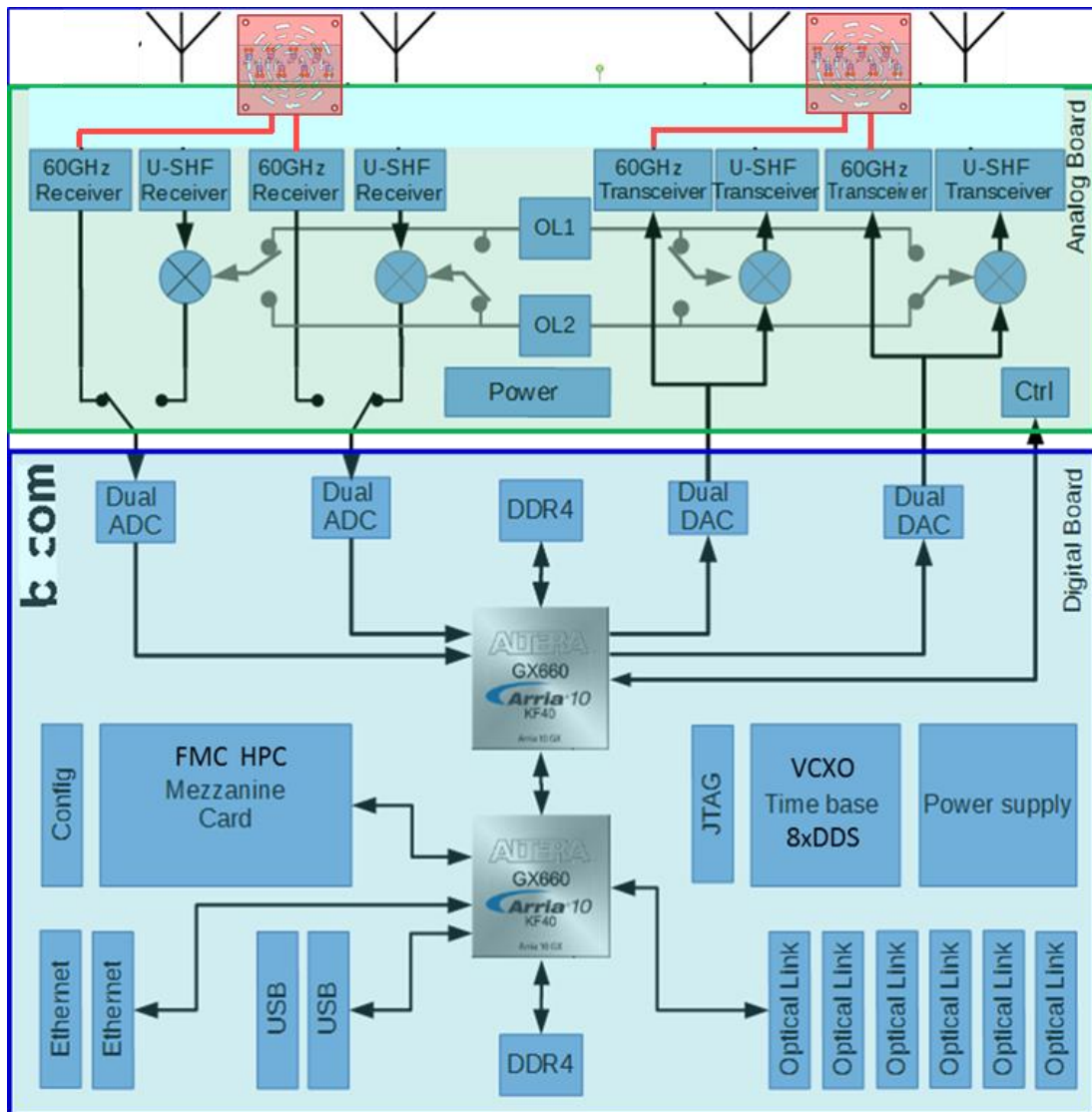


Figure 12: Analog and digital part of the platform schematic.

As illustrated in the Figure 12, the red area corresponds to MIMO 60 GHz antenna array considering beam steering MIMO antenna, focusing the transmit signal in a specific direction.

3.1.2 Digital board

The processing and interconnection capabilities of the digital board are mainly based on two midrange ARRIA 10 programmable FPGA chips from Intel / Altera. In addition to their combined computing capabilities, the association of these two FPGAs (named A and B in Figure 13), located respectively in the upper and lower parts of the digital board, provides connectivity to many signal processing and broadband interface functions.

The digital board includes the main following components:

Table 5: Digital board main components

Item number	Description
2x	FPGAs Arria 10AX066K3F40
4x	1Gbx8 DDR4 RAM
1x	Ultra low phase noise VCXO 125 MHz
2x	Quad DDS 500 MHz
2x	Dual ADCs with sampling rate up to 2.6GHz
2x	Dual DACs with sampling rate up to 2.4GHz
6x	4 high speed full duplex optical links (6x 40Gbps)
2x	1 Giga-bit Ethernet links
2x	USB links
1x	FMC HPC (100 Gbps XCVR + 58 Gbps LVDS) expansion port for general-purpose daughter board. Programmable power supply.
4x	HSMC connectors for interfacing with RF board or other miscellaneous (jumper, switches, LED indicators, IOs for control ...)

If required, a CPU can be implemented inside the FPGAs as a soft core.

Figure 13 and Figure 14 show in detail these elements respectively on front and rear view.

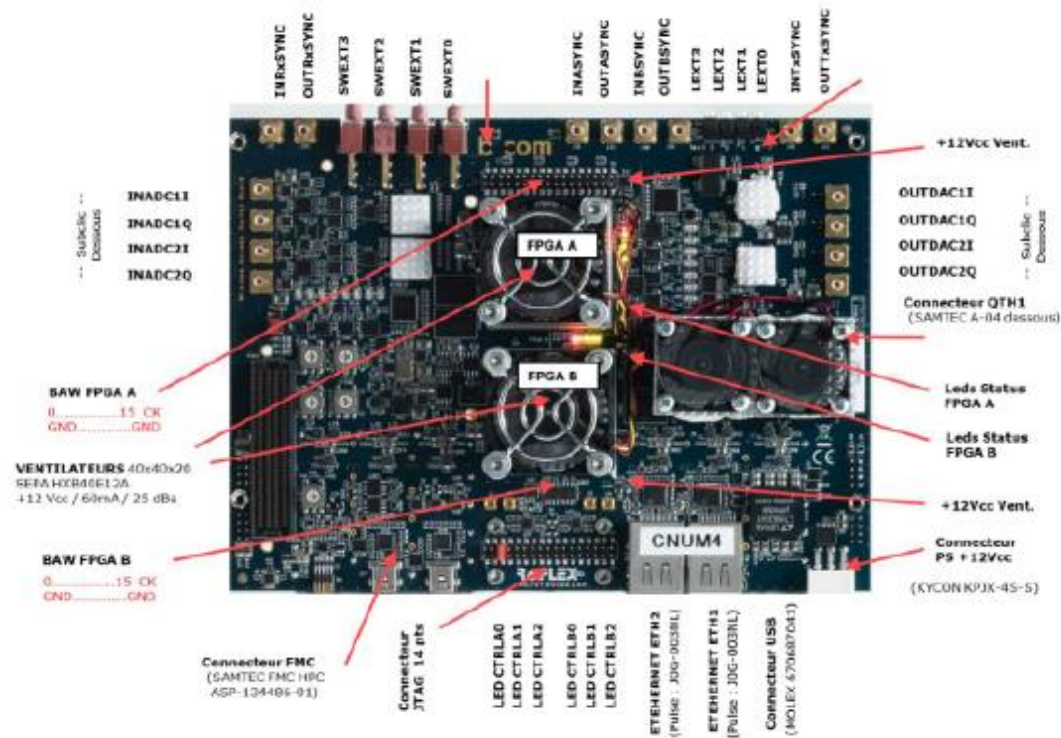


Figure 13: Digital board front view.

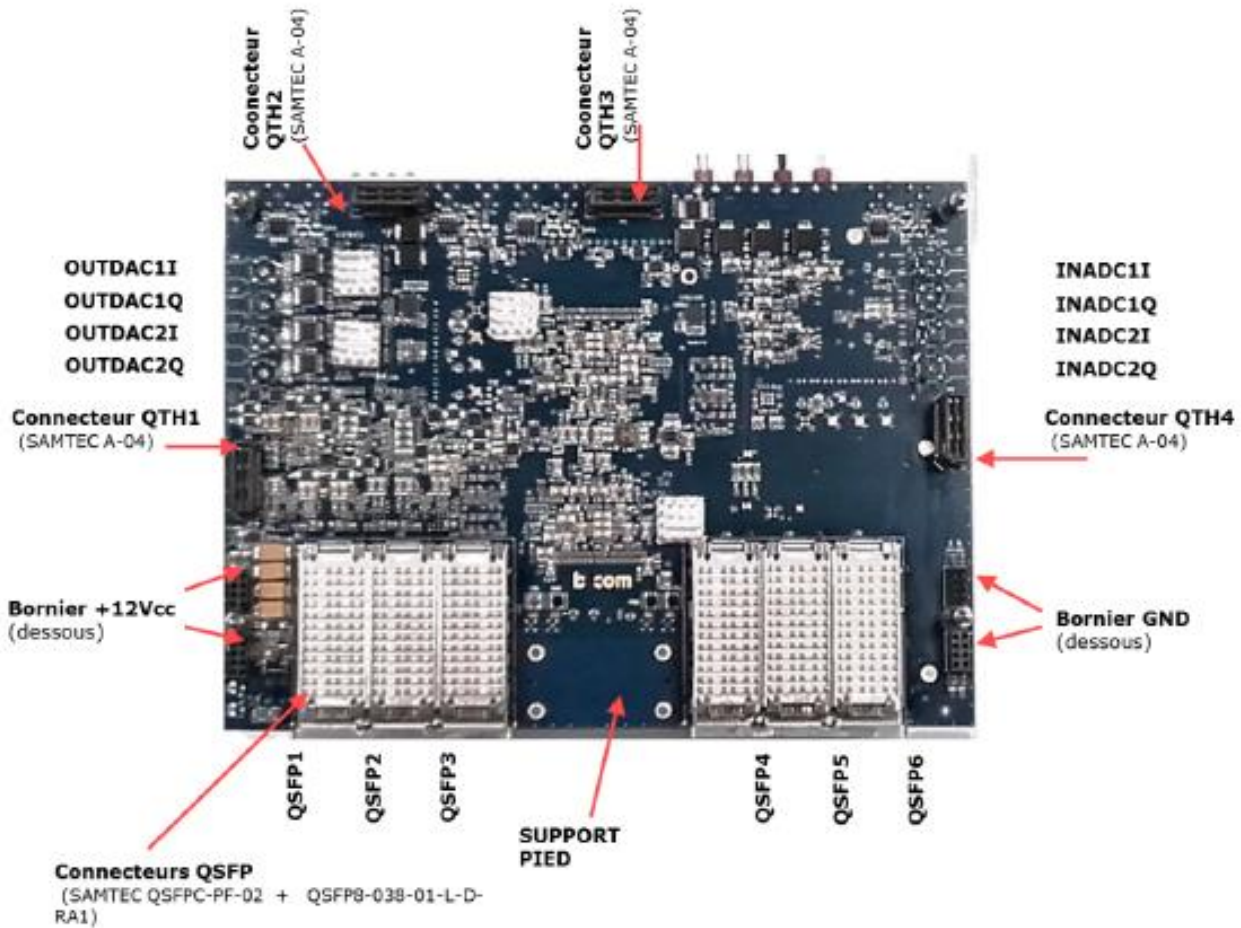


Figure 14: Digital board rear view.

3.1.2.1 FPGA connections

These FPGAs are widely interconnected and in accordance with Figure 12, the functions available on the board are linked to the FPGAs as follows:

- FPGA B mainly controls 6 full-duplex QSFP 40G modules for aggregated throughput of up to 240Gbps. It also supports two 10/100/1000 Ethernet ports, two mini USB 2.0 ports and two DDR4 1Gbx8 RAM modules for processing memory requirement. Finally, FPGA B is connected to a FMC HPC connector for future developments. Additional connections to the FPGA are provided as
 - 34 user-defined differential IO (LPC)
 - 80 user-defined differential IO (HPC)
 - 10 serial transceiver pairs (10Gbps each, full duplex)
 - 2 dedicated clocks
 - Power IO with adjustable voltage capability
- FPGA A is more dedicated to the A/D and D/A signal conversion and makes it possible to interface and manage:

- 2x Dual ADCs with 2GHz sampling rate each on 14 bits resolution
- 2x Dual DACs with 2GHz sampling rate each on 16 bits resolution

FPGA A also controls the RF board using HSMC interconnections and thus allows the configuration of all the main functions of the radio frequency transceivers of the RF board. As for FPGA B, two 1Gbx8 DDR4 RAM modules are dedicated to the FPGA B in order to be able to typically fulfil the physical layer processing algorithms requirements.

- FPGA A and FPGA B are also interconnected through a 50 Gbps full duplex link that allow the data transfer from the analog section to the optical interconnection for example and vice et versa.

3.1.2.2 Power supply

The power supply of the different functions and integrated circuits of the board requires no less than ten different voltages. Most of them are DC-DC converters based, powered by a single +12V supply voltage. However, for some functions that are sensitive to power supply noise, such as analog amplifiers or low noise phase clock synthesizer, linear regulators are used.

3.1.2.3 Clock tree

The clock system is based mainly on a 125 MHz VCXO clock source with very low phase noise and which can be synchronized to a 10 MHz reference signal or a 1PPS signal from a GPS receiver. In addition, the digital board has two accurate clock synthesizers (one for each FPGA) with four programmable clock output each. It also hosts two high frequency PLLs used as external sampling clocks for ADCs and DACs. Figure 15 shows a block diagram of the clock tree on the digital board.

Multi-RAT platform clock tree

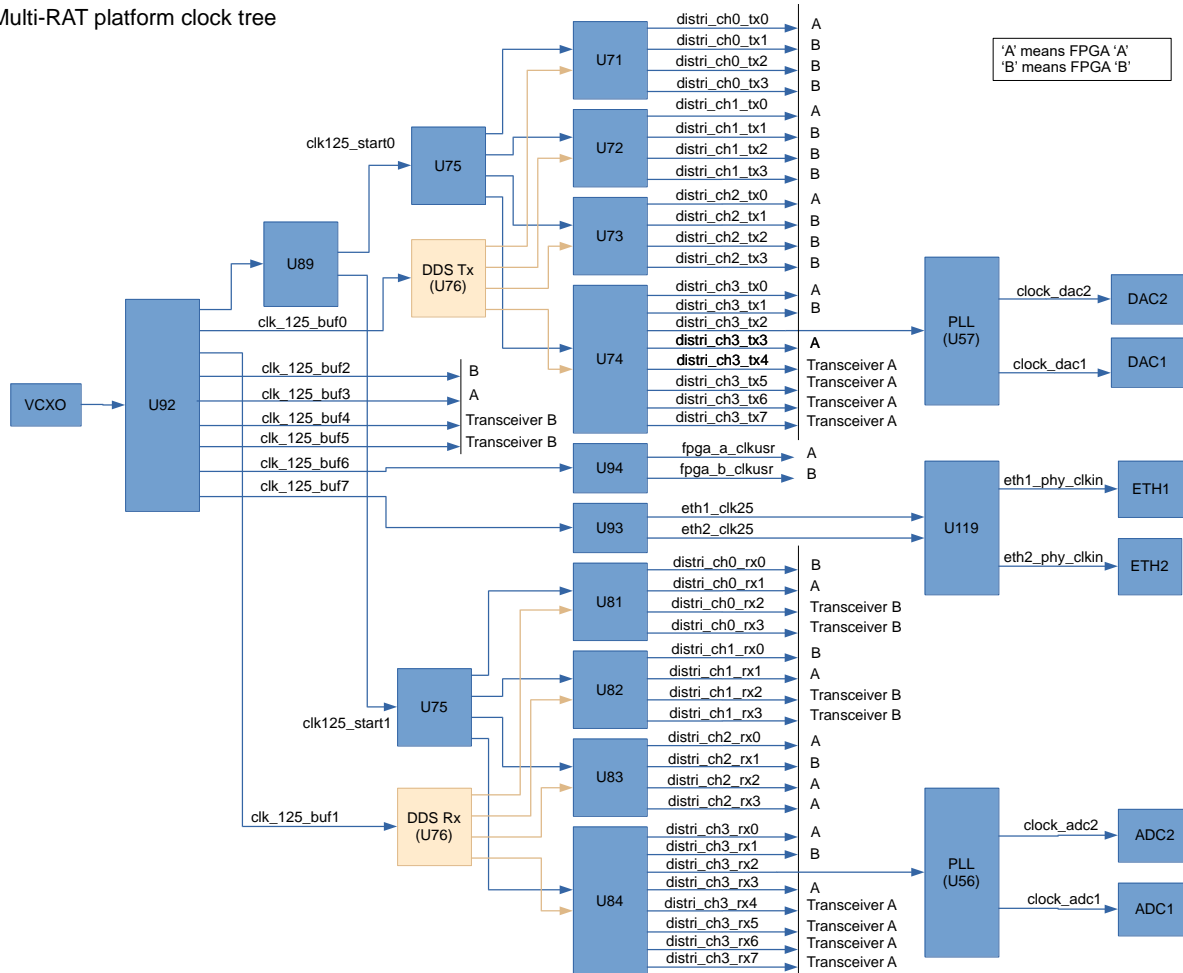


Figure 15: Multi-RAT platform clock tree.

3.1.3 Analog board

According to Figure 12, the RF board hosts two independent transmission-reception chains, as well as two distinct LOs which can be used by either of the two Tx or Rx functions. This is possible thanks to the implementation of a switch matrix. Therefore, depending on the application, a MIMO transceiver can use the same frequency for transmission and reception, but also two distinct frequencies, with different standards and bandwidths as well. Frequency aggregation of bands is also possible, combining either low or high frequencies. The millimetre waves part consists of two mezzanine cards, dual Tx and dual Rx, plugged on the RF board. They host dedicated integrated circuits from Analog Devices / Hittite, and take advantage of the LO synthesis of RF and digital boards.

On the other hand, the 70 MHz - 10 GHz part is designed with discrete components, based on elementary functions, and a Zero IF operating principle is implemented. This avoids using an intermediate frequency to generate or receive the transmission channel. The advantage of this is its simplicity of implementation, but its main drawback is the imbalances between the two I and Q channels of the complex signal. However, thanks to efficient signal processing algorithms in the digital domain, it is possible to greatly minimize the effects of this imbalance.

For the generation of the in-phase and quadrature components of the modulation / demodulation carrier frequency, T-flip-flop pairs have been used for each clock components. The main clock is generated by a VCO, of variable frequency

on at least one octave, and the exact carrier frequency, at least half of the output frequency of the VCO can be obtained by frequency division and shift of the VCO controlled by the digital board.

3.1.3.1 RF board

The operating principle which makes it possible to continuously generate a transmission channel over a very wide frequency range, is represented in Figure 16 for the two TXs of the RF board. According to the Zero IF principle, the demodulation processing is entirely symmetric to the transmission processing and is shown in Figure 17.

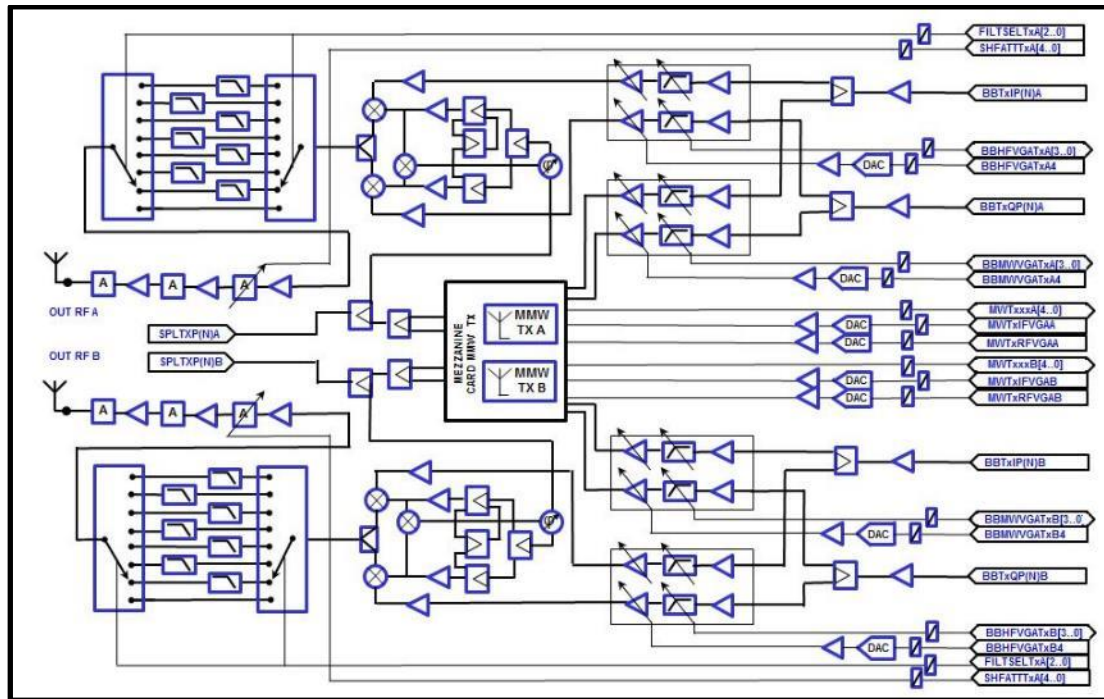


Figure 16: Tx schematic of the RF board.

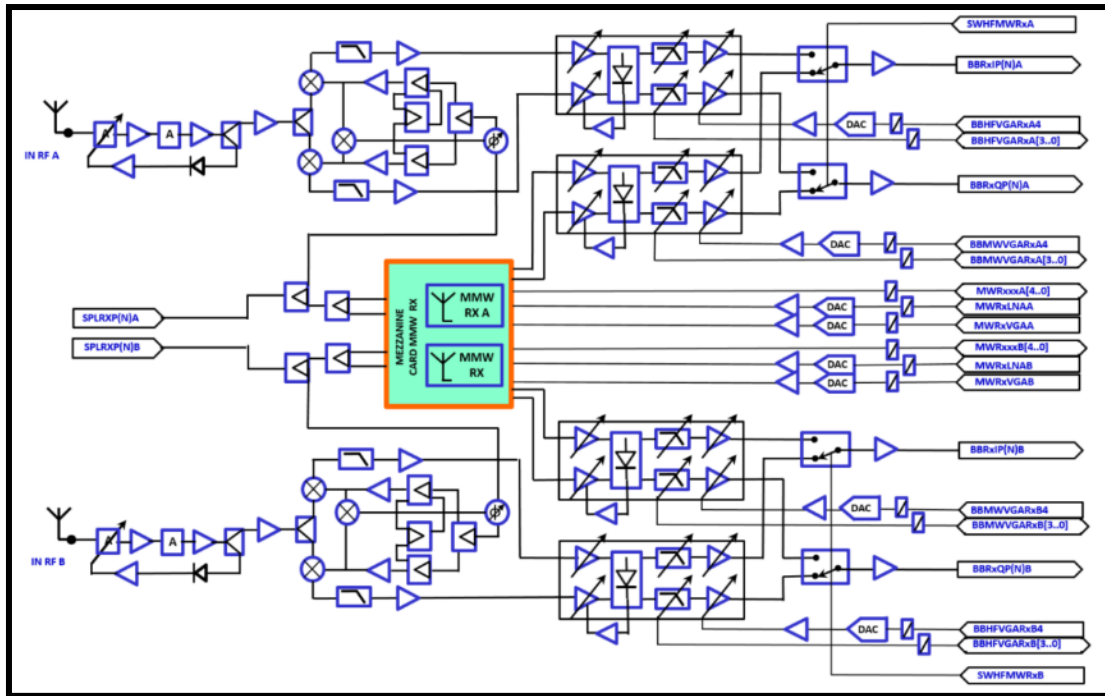


Figure 17: Rx schematic of the RF board.

Figure 18 gives examples of what kind of signal can be synthesized with the RF board. On the left a 700 MHz bandwidth baseband signal spectrum is shown, and on the right a 600 MHz bandwidth RF signal at 2.5GHz.

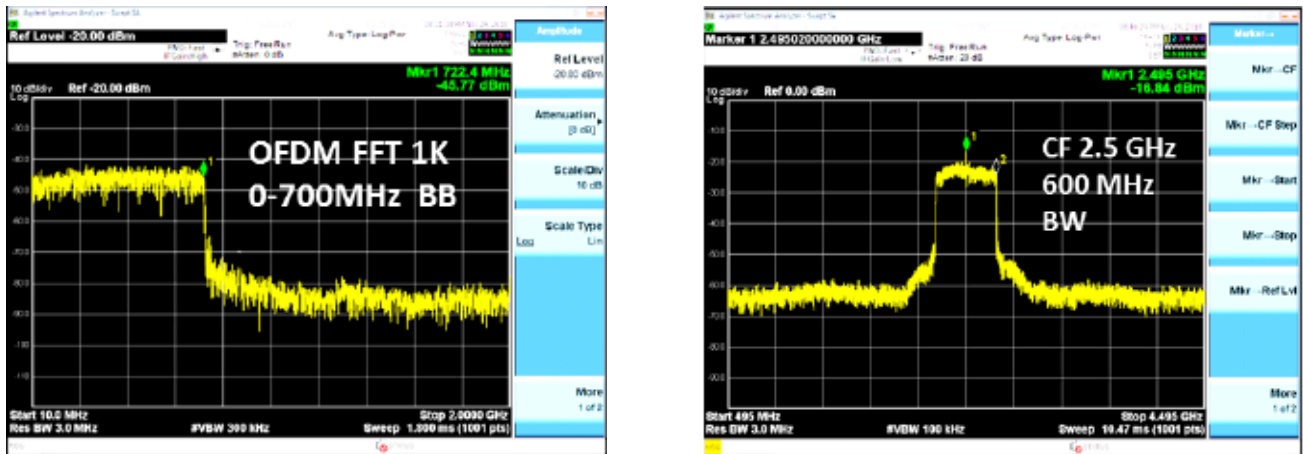


Figure 18: Base band and radio signal example.

Figure 19 shows examples of the quality of the LO signals. On the left the phase noise at 200kHz of the reference oscillator is shown, and on the right the phase noise at 100kHz.

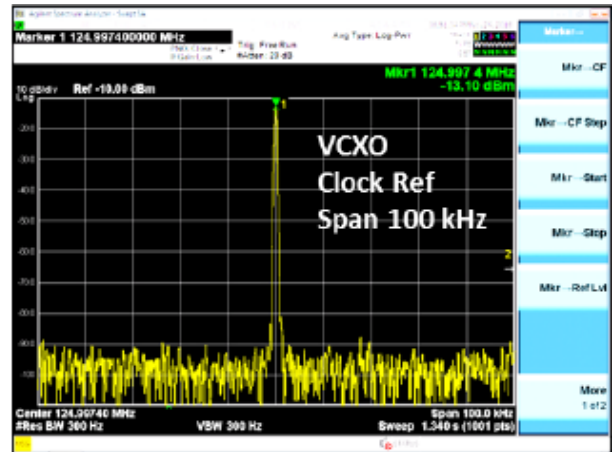
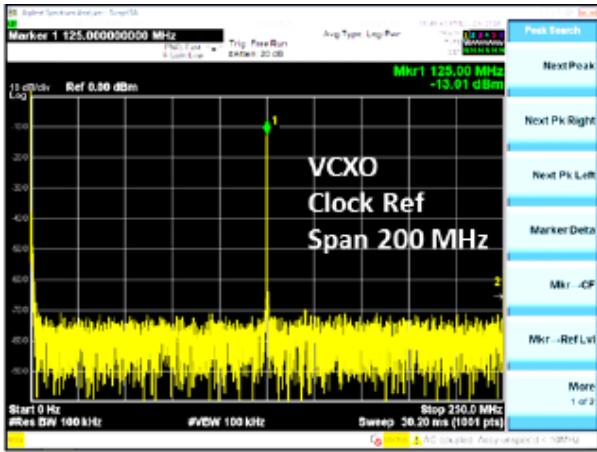


Figure 19: Base band and radio signal example.

3.1.3.2 Radio board hardware

The RF board includes the main following functions:

- 2x fully independent zero IF transmitter (75 MHz – 10 GHz)
- 2x fully independent zero IF receiver (75 MHz – 10 GHz)
- 1x fully independent ultra-wide band VCO (10-22 GHz)
- 1x HSMC connector for millimetre wave daughter board with two independent transmitters
- 1x HSMC connector for millimetre wave daughter board with two independent receivers
- 4x HSMC connector for digital board interconnection

Figure 20 and Figure 21 show in more details these elements respectively on front and rear view.

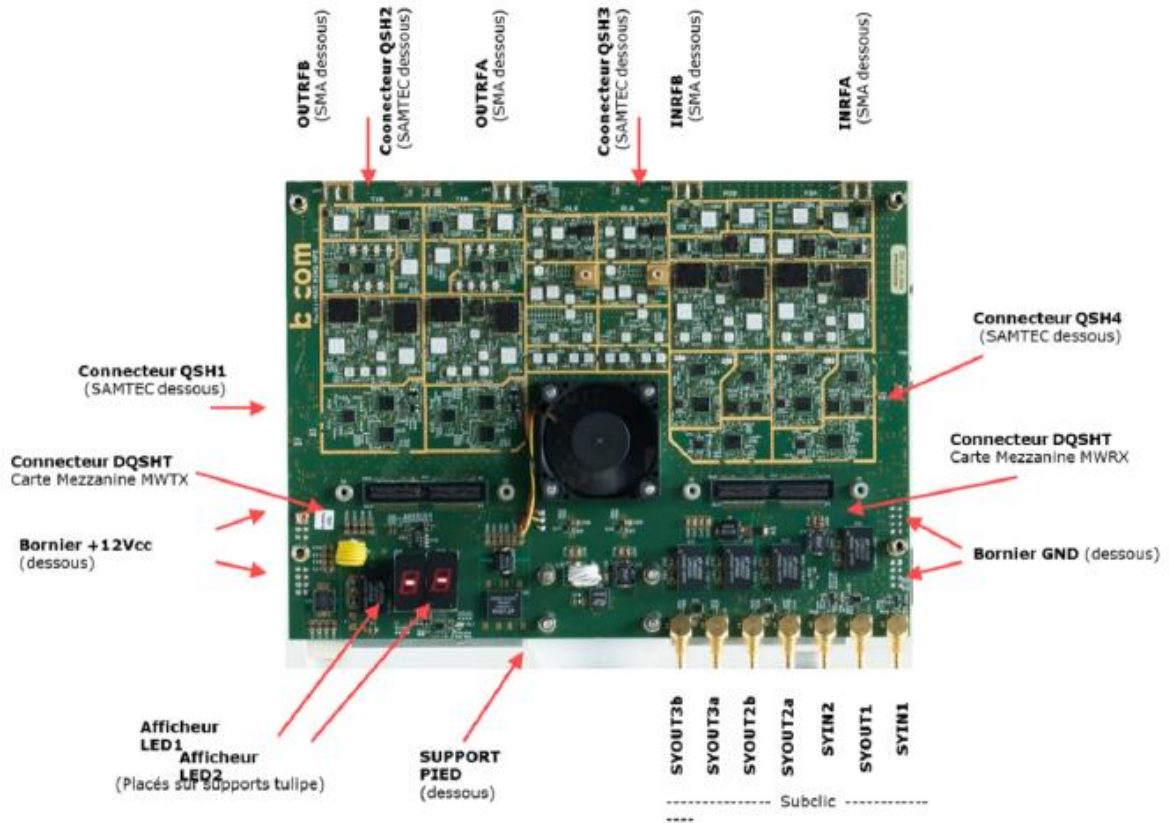


Figure 20: Analog RF board front view.

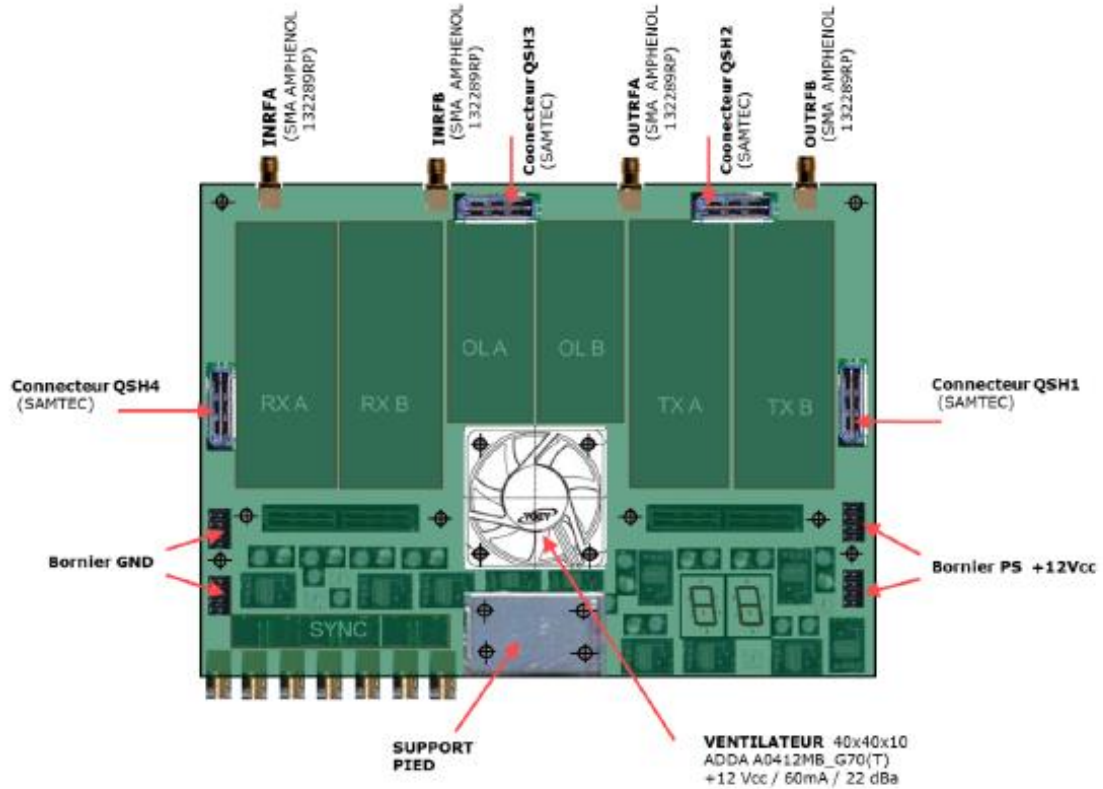


Figure 21: Analog RF board rear view.

3.1.4 28GHz board

This board is under construction, and no hardware is ready yet. This will use direct up and down conversion using the local oscillator generated by the RF board and by two multipliers to reach the desired frequencies.

3.1.5 60GHz board

This board is under construction, and no hardware is ready yet. To reach such high frequency signal, with a large bandwidth dedicated circuits from Analog Devices will be used for up and down conversion. The HMC6300 is well suited for the transmitter side. In order to offer MIMO transmission, a bundle of transmission channels is available on a single board. Each of these drives a dedicated patch antenna and a phase shifting process allows beam forming to improve the link budget and the receiver tracking. A similar board is under design for the receiving side. The HMC6301 component from AD realizes the down conversion, and as on the transmission side, a set of 8 receivers, connected to dedicated patch antennas allow MIMO reception with beamforming and tracking.

3.1.6 Optoelectronic board

To enlarge the physical propagation channel choice, an optical board is under design. Once again, the board is under design and no hardware is ready for the moment. For this board, IR wavelengths are selected, and wide band modulation are required to allow a high data rate transfer. Two mezzanine boards are under development(see Figure 22), one for the transmission, one for the reception. As signals from digital board are complex and coming from a dual DAC, each portion of the signal drives a dedicated laser diode, one at 940nm, and the other one at 850nm. This way it is possible to transmit two modulated signal independently for the OFE.

Regarding the receiving board, both wavelengths will be received simultaneously to keep the wide bandwidth capability. Additionally, to avoid mutual channel interference and improve the overall SNR, a narrow band optical filter will be used in front of each reception components.

Finally, to reach a high SNR on the receiver, (and guarantee a long-range link quality), instead of using a single large APD (with a high sensitivity, but poor SNR), a matrix of smaller APDs are considered. This way, the high bandwidth and sensitivity is preserved.

Figure 22 shows an overview of the boards and the main advantages of the optical transmission chain.

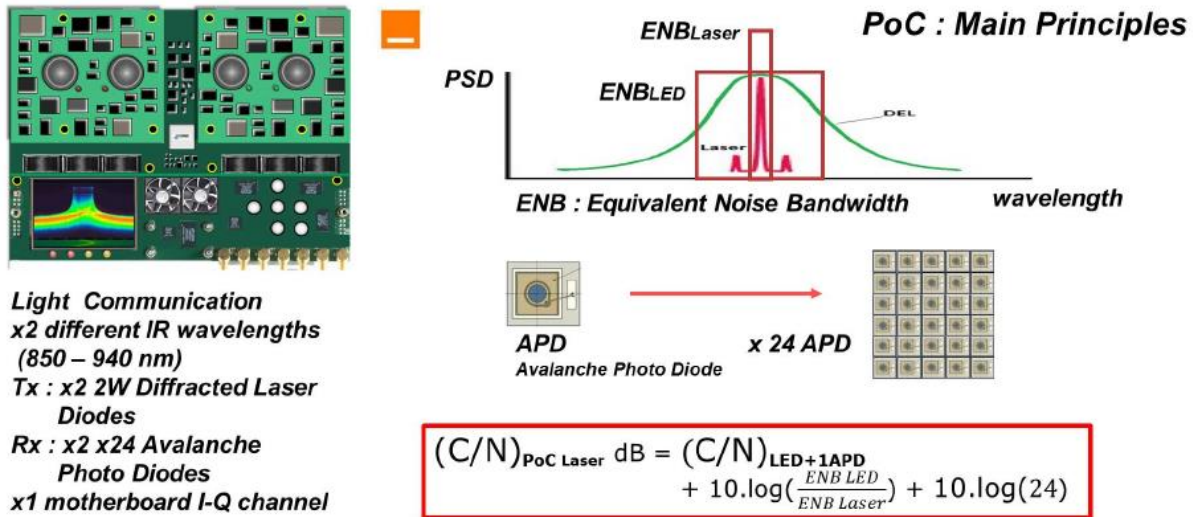


Figure 22 : Optical Tx and Rx mezzanine boards / main advantages.

Figure 23 shows the main characteristics of 850 nm emission laser diodes under consideration. The 940 nm characteristics are similar if considering the wavelength dispersion, the diffraction, and the spatially the modulation speed. As far as eye safety is concerned, power levels for class 1 operation are still to be determined. The source incorporates a diffuser, which potentially increases the allowed power which can be emitted, but more detailed work is required to ensure a class 1 certification can be obtained.

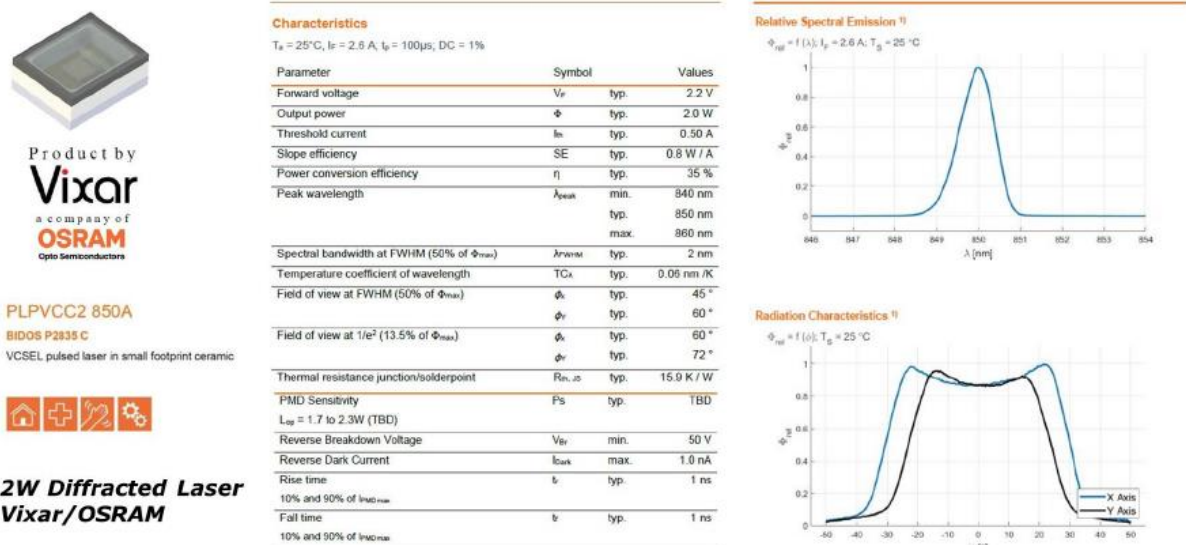


Figure 23 : 850 nm Tx diffracted laser diode.

Figure 24 defines the useful laser input voltage modulation range to keep a linear relation with the modulated output power. If required, a slight pre-correction could compensate some non-linearity and keep the modulation range the widest.

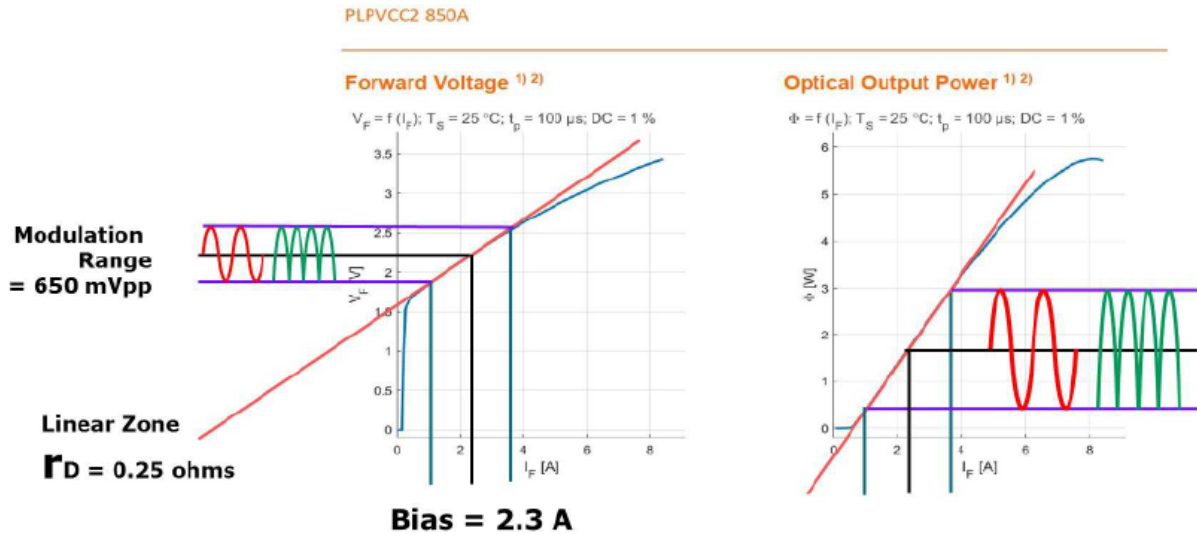


Figure 24 : Tx laser diodes driving mode.

Figure 25 show the laser diode modulation principle. As usual, each diode is driven by a real signal positive signal. Nevertheless, in our case, modulated signals do not comes from classical OOK modulation, but from OFDM. Some additional signal processing is required to ensure the complex to real translation to keep the real only signal. The figure also shows a typical driver architecture for laser diodes and the dispersion emission angle that have the diodes (by construction), $\pm 20^\circ$ vertically and $\pm 30^\circ$ horizontally.

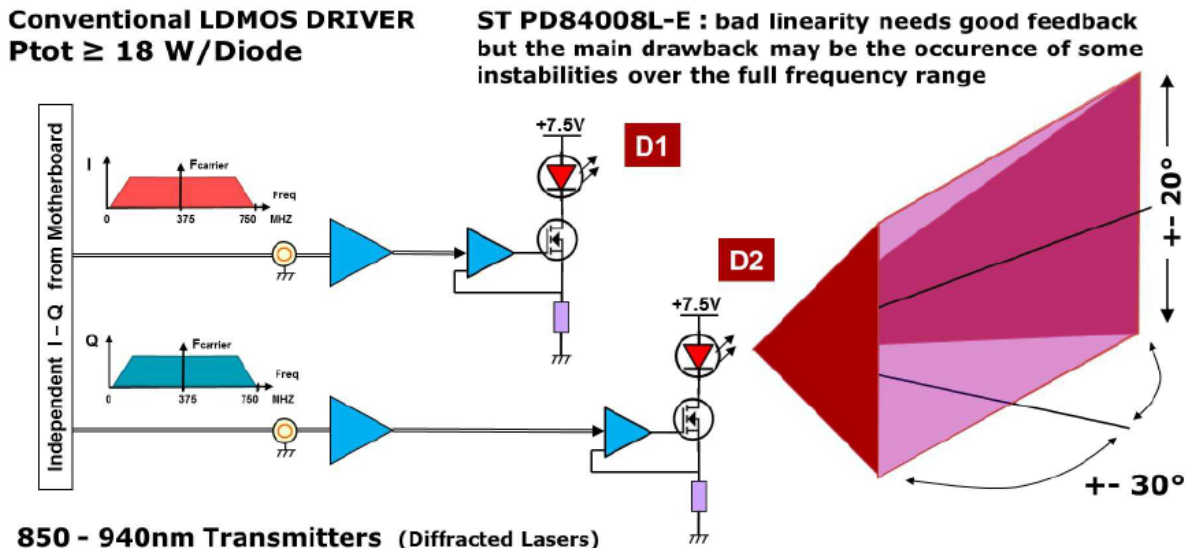


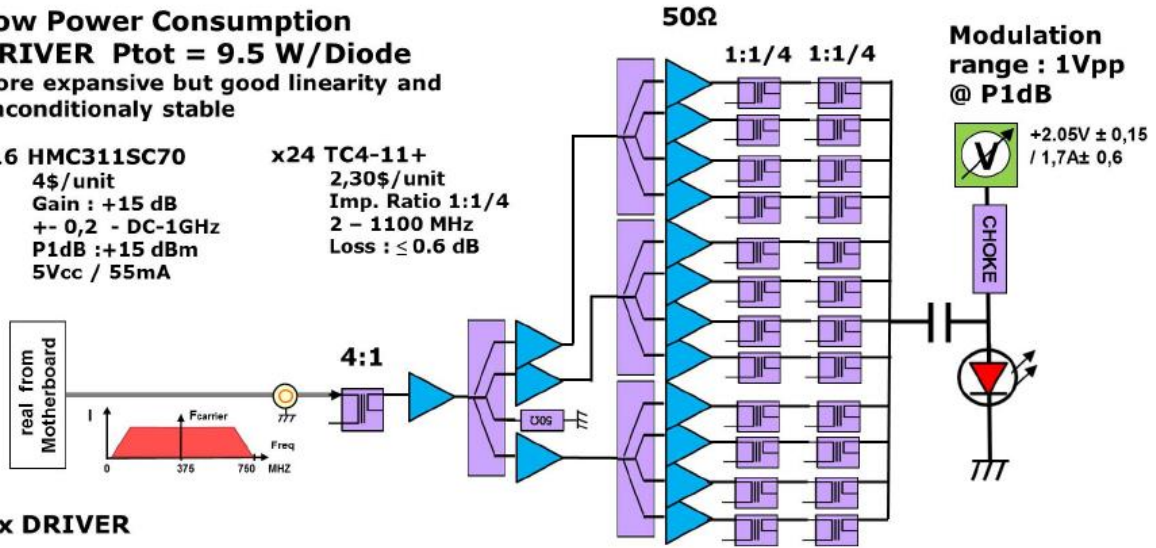
Figure 25 : Tx laser conventional driver / diffracted characteristics.

Figure 26 shows the power efficient architecture for the laser drivers, allowing reduced heat sinking and stable operation

Low Power Consumption DRIVER Ptot = 9.5 W/Diode
 More expansive but good linearity and unconditionally stable

x16 HMC311SC70
 4\$/unit
 Gain : +15 dB
 + 0,2 - DC-1GHz
 P1dB : +15 dBm
 5Vcc / 55mA

x24 TC4-11+
 2,30\$/unit
 Imp. Ratio 1:1/4
 2 - 1100 MHz
 Loss : ≤ 0.6 dB



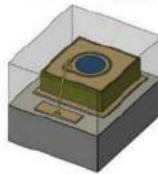
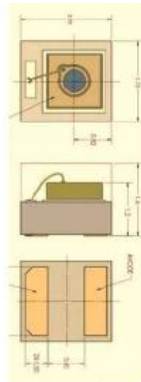
Tx DRIVER

Figure 26 : Tx laser low power consumption driver used mode.

Figure 27 show main characteristics of selected APD. Their main advantage is their wide modulation bandwidth, but consequently, their receiving area is small. This limits the received optical power and could significantly reduce the communication distance.

To mitigate this limitation, the utilisation of many APD is considered. This increases the collection area and therefore improves the SNR.

Parameter	C30737PH-500-80 C30737CH-500-80 C30737MH-500-80 C30737EH-500-80			Unit
	Min	Typical	Max	
Active Area Diameter		500		µm
Peak Sensitivity Wavelength		800		nm
Breakdown Voltage, V _{BR}	120		210	V
Temperature Coefficient of V _b , for Constant M	-	0.5	-	V/°C
Gain (M) @ 800nm	-	100	-	
Responsivity @ 800 nm	-	50	-	A/W
Total Dark Current, I _d	-	0.1	1	nA
Noise Current, I _n , f=10MHz, Δf=1 GHz	-	0.1	-	pA/√Hz
Capacitance, C _j	-	2	-	pF
Rise + Fall Time, R _f = 50 Ω, 10%-90%-10% points	-	0.3	-	ns
Cut-off frequency (-3 dB)	-	1.3	-	GHz
Storage Temperature	-50		+100	°C
Operating Temperature	-40		+85	°C



C30737PH, CH, MH and EH Series
 Epitaxial Silicon Avalanche Photodiodes – Through-hole and Leadless SMT packages

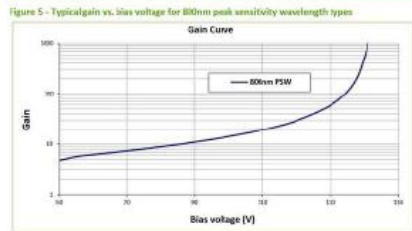
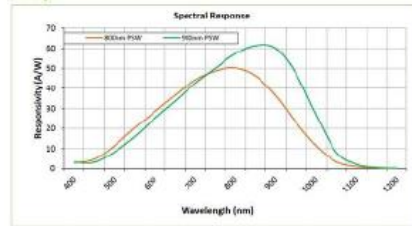


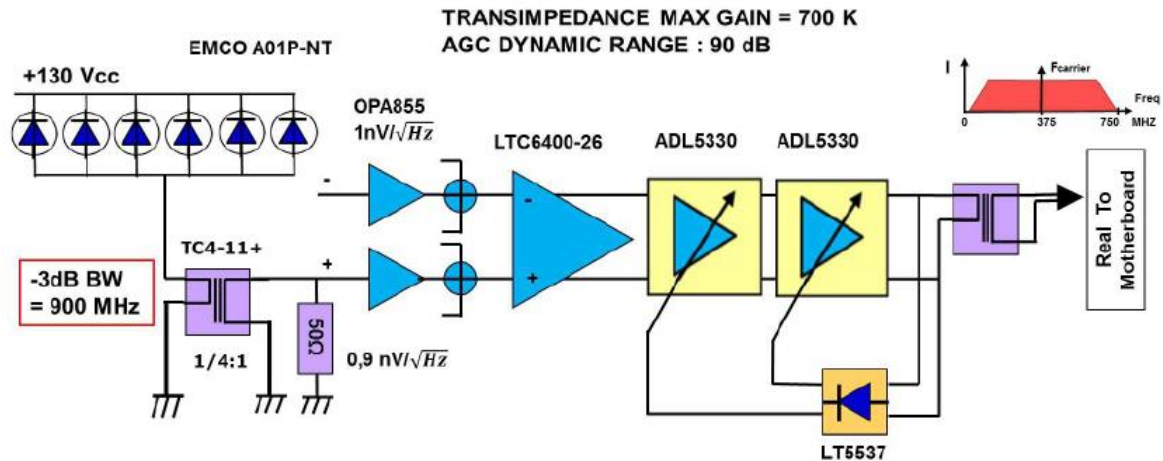
Figure 3 - Typical Responsivity vs. wavelength.
 800nm PSW – APD with 800nm peak sensitivity wavelength; 900nm PSW – APD with 900nm peak sensitivity wavelength



Avalanche Photo Diode
 excelitas-technologies

Figure 27 : Rx Avalanche Photo Diode.

As an illustration, Figure 28 show how the APD array could be aggregated and how the current to voltage conversion is achieved, whilst keeping the noise floor as low as possible. A final automatic gain control would keep the signal in the correct range for optimal sampling process.



IR Receiver Principle

Figure 28 : Rx preamplifier synoptic.

The analog board hosts both IR Tx and Rx daughter boards. If two transceivers are used, one for the access point, and the other for the user for example, a full duplex transmission can be implemented. Half duplex can also be achieved as there is no interaction between Tx and Rx module of a transceiver. Additionally the downlink can be realised with optical modules, and the uplink could be realised with another wireless technology.

3.2 Theoretical link budget

In order to get an estimation of the resulting optical system throughput, we need to get an estimation of the SNR on the optical receiver, an estimation of the constellation that could be used considering this SNR, and the resulting throughput with the OFDM frame structure.

3.2.1 Optical link budget

Using reference characteristics from the components datasheet, and using basic signal processing, the following theoretical values are obtained

Table 6: Tx theoretical results

Parameter	Value
Linear voltage modulation range on the laser diode input	650mV
Modulated radiant flux	0.93W
Modulated flux density at 5m	54mW rms / m ²

Receiver optimisation suggests that 6 groups of 4APDs is the best configuration and this is considered in Table 7.

Table 7: Rx theoretical results

Parameter	Value
Total receiving area for x4 APD group	7.8.10 ⁻⁷ m ²

Filter transmission min	70%
Responsivity	50A/W
Total rms current for x4 APD group	1.47 μ A
Total rms voltage for x4 APD group after transformer	36 μ V
Total dark and thermal noise /50Ohms for x4 APD group	2.9 μ V
SNR for x4 APD group	22dB
Total SNR at 5m BW(x6 x4 APD group)	26.5dB

3.2.2 LDPC performance

LDPC codes are part of iterative decoding algorithms which increase performance with a latency and/or hardware resource cost. An LDPC decoder has been designed to decode codewords, with the capability to process 32 soft bits at a clock speed of 250 MHz, leading to 8 Gbps throughput. With such a structure, decoding latency stays below 0.5 μ s. The structure is directly linked to the chosen matrix (a WiMax one) to keep good decoding performance (see Figure 29) with reasonable duplication (see Figure 30).

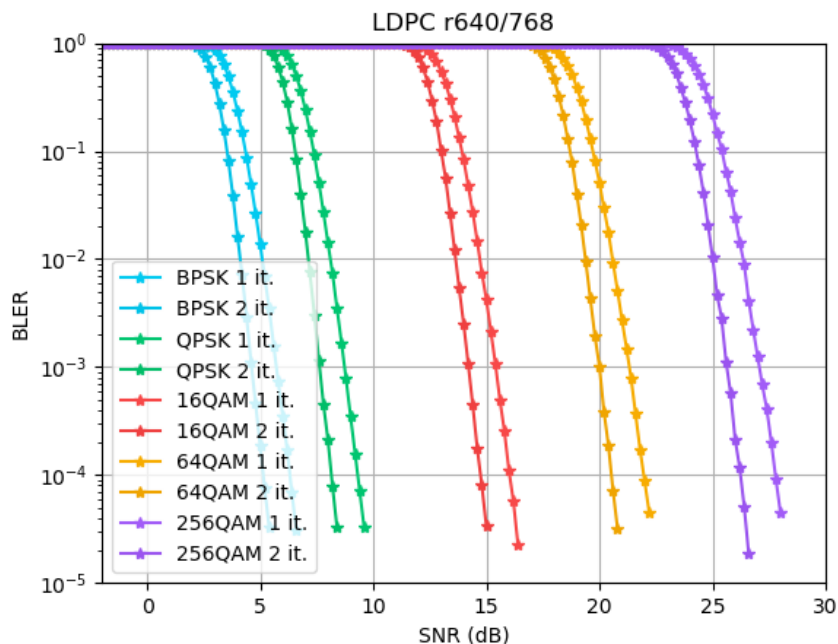


Figure 29: LDPC performances vs SNR, for 1 or 2 iteration, from BPSK to 256QAM

The iterative decoding process finds and corrects errors in the received message by applying the correction process many times. If only one instance of the decoder is used, the overall throughput of the decoded stream will be TP_{max}/N where TP_{max} is the maximum throughput of the decoder and N the number of times the data goes through the decoder.

To overcome this limitation, an optimised structure of the decoder is designed to reach 8Gbps and if N iterations are required, N instances of the decoder are used (see Figure 30), keeping the overall throughput at its maximum.

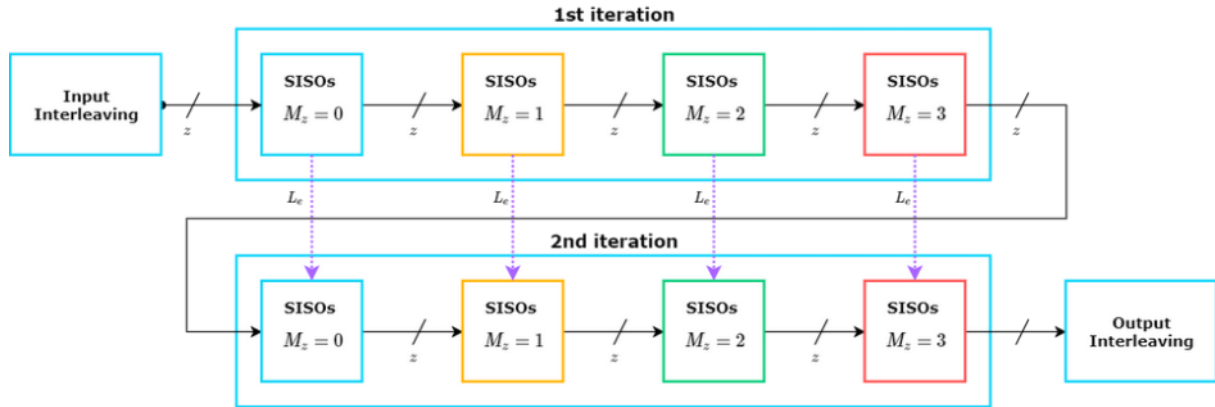


Figure 30: LDPC decoding architecture

With the theoretical SNR of 26.5 dB seen in 3.2.1, the 256QAM could be achieved, eventually using a third iteration. However, the effective SNR should be a bit smaller, and a third iteration on the FPGA requires a lot of resources. So in this case mappings up to 64QAM are considered

3.2.3 OFDM frame structure

As described in the D4.3 : Common Analog and Digital Baseband Design for Flexible Radio and Optical Transceiver we consider the OFDM frame definition given in the following table:

Table 8: OFDM physical layer parameters

Frame parameters	Value
Channel bandwidth (MHz)	1966,08
FFT size	4096,00
Subcarrier Spacing (KHz)	240,00
FFT period (ns)	4166,67
GI length (ns)	297,04
OFDM symbol length (ns)	4463,71
Pilot nb	3134,00
Null SubCarrier nb	2,00
Used Bandwidth (MHz)	752,64
Frame length (μ s)	499,94

3.2.4 System throughput

Considering modulation up to 64QAM, a 5/6 coding rate LDPC code and some data used in the frame as data header, the throughput that could be achieved for a single optical link is presented in Table 9.

Table 9: Estimated output throughput for a single optical link

Bloc	TP
ADC output (MSps)	1966,08
IFFT Output (MSps)	918
Equalisation output (MSps)	652
De-mapper QPSK output (Mbps)	1304
De-mapper 16QAM output (Mbps)	2608
De-mapper 64QAM output (Mbps)	3912
FEC QPSK output (Mbps)	1032
FEC 16QAM output (Mbps)	2065
FEC 64QAM output (Mbps)	3097

3.3 Test results

Due to delay in the optical board delivery, and the new revision of the RF board, we are actually not able to provide any results of link testing. Results concerning other aspects of the system are presented here.

3.3.1 GUI

First, to be able to manage, configure or even debug some digital computations, a very useful tool is the graphical user interface.

3.3.1.1 Low level control

As the developed system is complex (more than 2000 32bits wide registers can be configured), a GUI is developed to control the low level parameters including OFDM ADC, DAC, clock references, DDR, LDPC and FPGA parameters.

Figure 31 shows some parameters of the OFDM configuration in the GUI, but also all the tab that gives access to peripheral control and status.

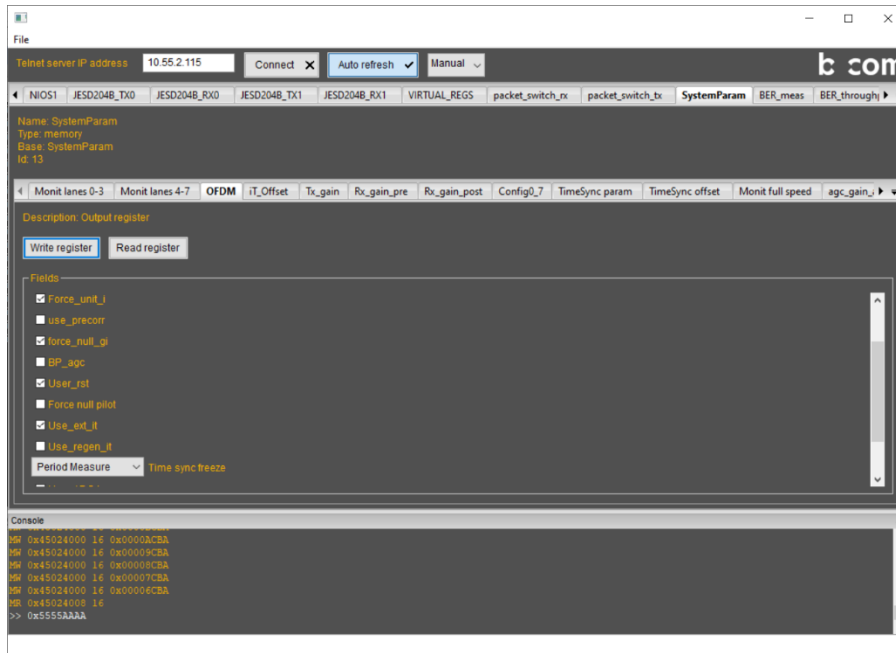


Figure 31: ODFM control GUI : OFDM Tab

3.3.1.2 System control

A second GUI is also designed, but dedicated to the systems parameters. It allows to change the user number, a user bandwidth capability, the constellation used, or some of the PRBS data are used. This allows the link performance (BER) to be measured for all the types of link (RF or optical)

Here after an example of configuration defined by the system control GUI:

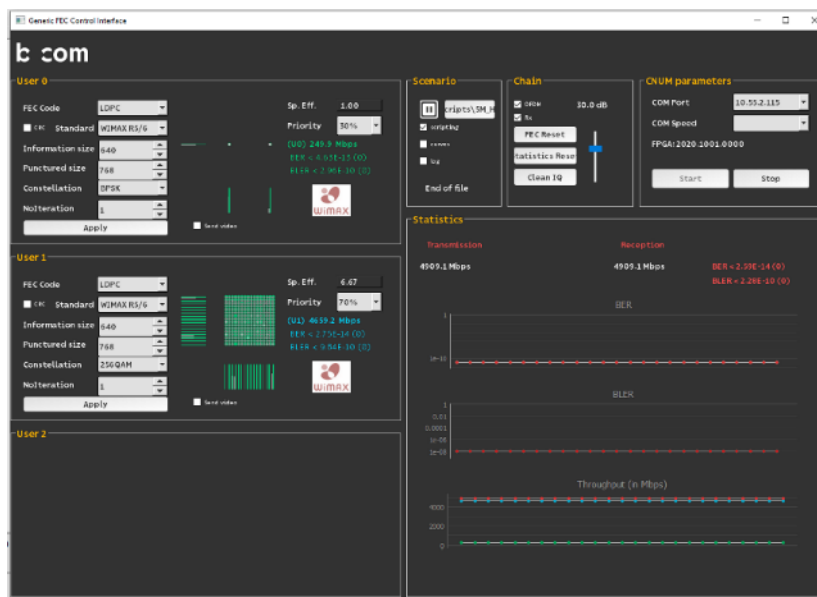


Figure 32: System control GUI

Two user windows can be seen, and a statistic one. The first allow changings of the LDPC parameters (locked to LDPC 5/6 in our case), the constellation used by each user (choice could be BPSK, QPSK, 16QAM, 64QAM or 256QAM), and the percentage of the overall bandwidth that can be used (in that case: 30% for the user#0, and

70% for the user#1). On the statistics panel, the overall received and transmitted data rate is displayed (4909.1 Mbps for that configuration), as well as graphical view of the link quality (BER and BLER).

3.3.1.3 Monitoring

A visualisation of generated signal is essential to check that all the system modules are well controlled, or to track some distortion along the receiving chain or to visualise the transmission channel (radio or optical) and then understand why such signal degradation.

This tool is developed using GNURadio, open source project, and thanks to correct configuration and the appropriate format of sample captured into the FPGA, we are able to display information as the incoming samples that comes from the ADC (Figure 33), or the receiver equalisation output (Figure 34). Some post processing are also used to compute, base onto the recovered samples, the channel impulse response or the incoming data signal bandwidth thanks to an software FFT.

The data are captured onto the FPGA as a continuous burst of data (8192 data points), and are exported to the PC with a slow data rate (1 Mbps) to preserve Ethernet bandwidth for user applications.

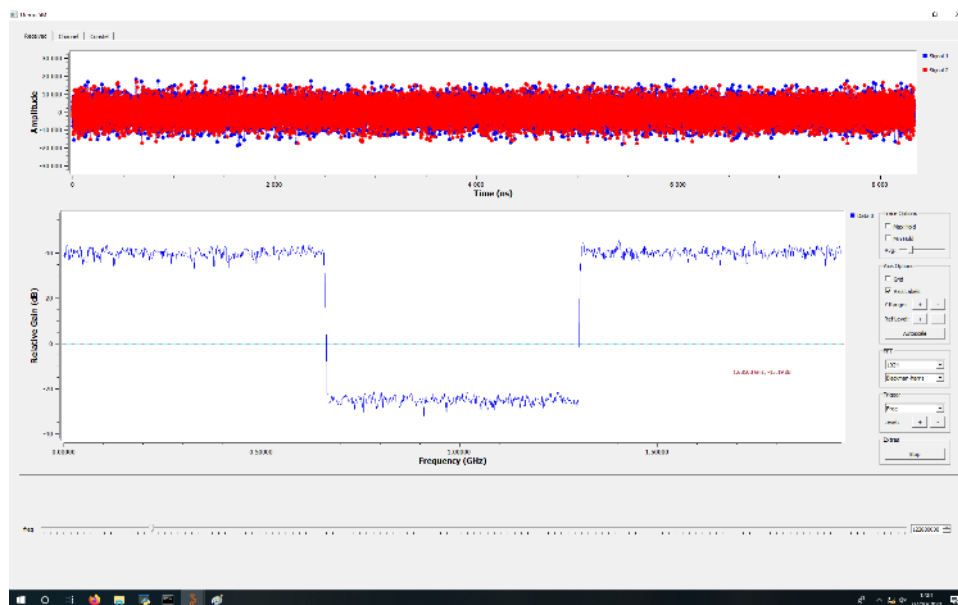


Figure 33: Monitoring GUI : received samples view

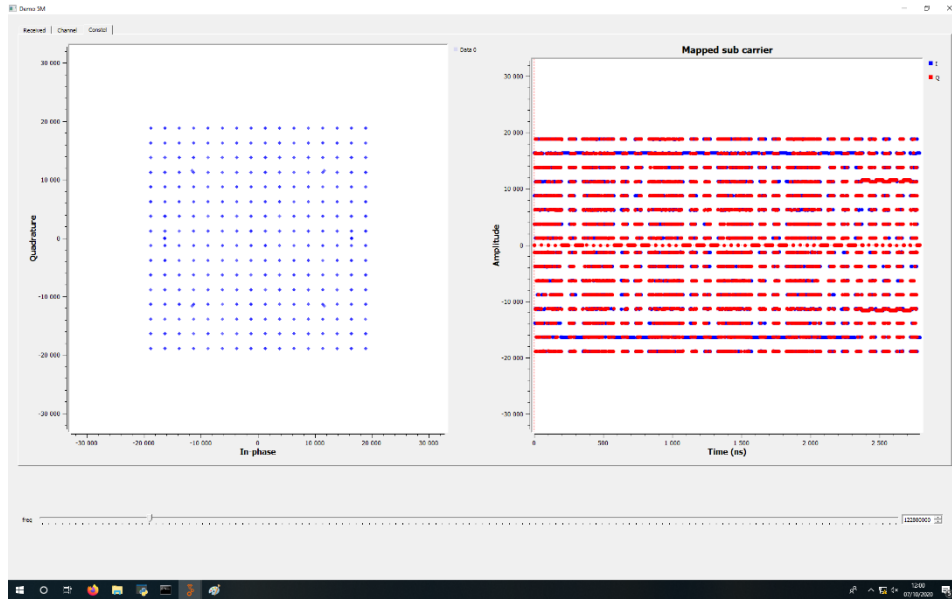


Figure 34: Monitoring GUI : de-mapping view (256QAM)

3.3.2 Digital section

All the specification originally planned are not yet implemented, but many of them are ready. Table 10 shows the features supported.

Table 10: Supported feature of the digital section

Feature	Supported
Ethernet Interface	1G (RJ45), 10G(SFP+), 40G (QSFP+)
Protocol	ARP, ICMP, UDP, Telnet, HTTP
User number	2
Bandwidth allocation	from 0 to 100% by 10% step
Constellation	BPSK, QPSK, 16QAM, 64QAM, 256QAM
LDPC iteration number	2
Sampling frequency	1966MHz
Base band signal bandwidth	1300MHz (2x650MHz on complex signal), 30dB SNR min on the overall BW

Using the digital system to generate a full OFDM signal, and a base band transmission (I/Q signal) link from Tx to Rx, we can use the monitoring interface to check the module performances, and the system GUI to check the overall system performance and capability.

In Figure 35, we can see the received signal from the ADC and the post processing FFT that show the received SNR for a base band link. Figure 36 shows the channel estimation output and the channel impulse response, and Figure 37 shows the de-mapping input.

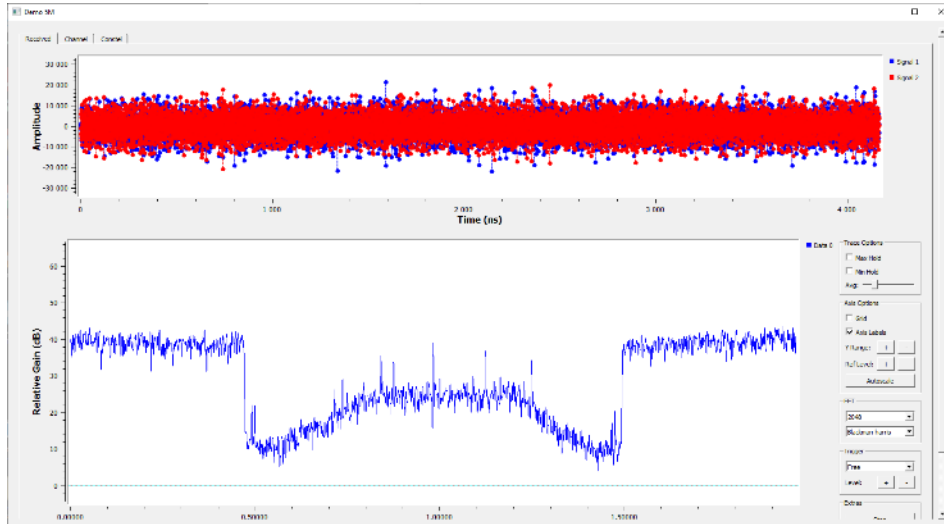


Figure 35: ODFM control GUI : ADC samples view (prefect channel)

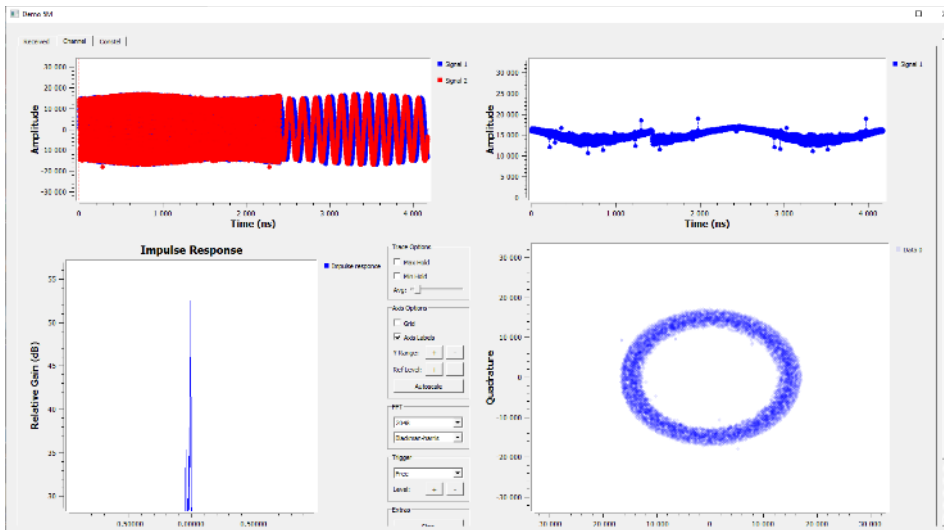


Figure 36: ODFM control GUI : channel estimation view

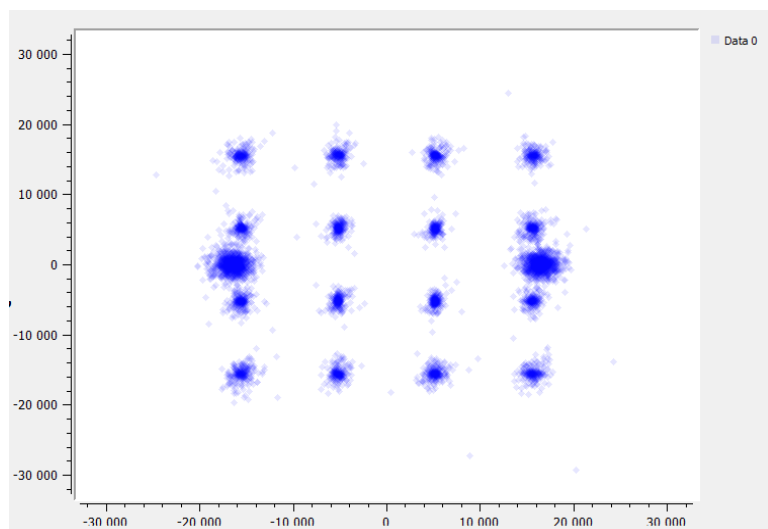


Figure 37: ODFM control GUI : de-mapping view with base band transmission

These are good results if we consider the wide bandwidth that is used. Imperfections such as channel flatness will be corrected in future work.

3.3.3 60GHz section

60GHz components were used to realise wireless transmission. Figure 38 shows a digital board associated with a 60GHz radiative element composed of a patch antenna, and a radio lens (a close-up view is shown in Figure 39) which concentrates the radio signal into a narrow beam, as an optical lens could do.

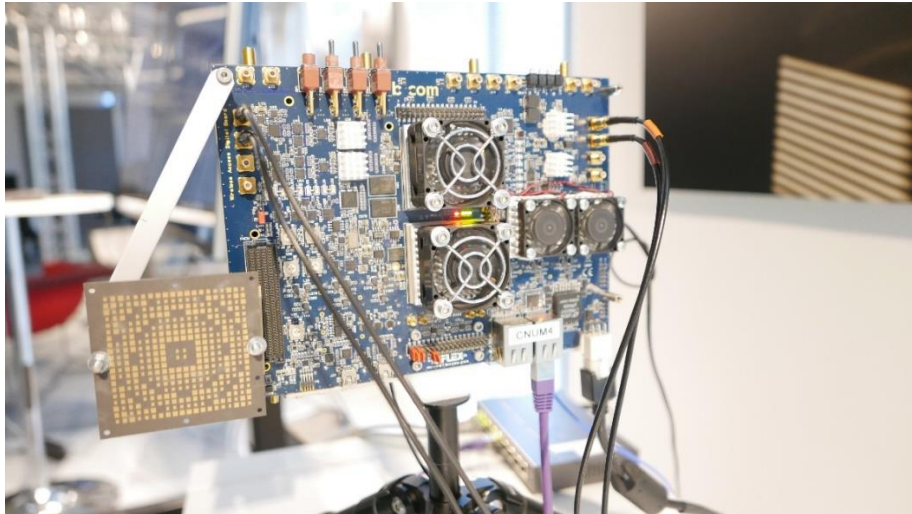


Figure 38: Modem with 60GHz patch antenna and focussing lens



Figure 39: 60GHz patch antenna and focussing lens

3.3.4 Hybrid full duplex transmission

Time limitations, and the delay to the optical board manufacture meant limited components were available. So, in order to realise a full duplex set up, we decided to realise the downlink with a 60 GHz transmission, and the uplink with a baseband transmission (with copper cables, I and Q). The following picture show the set up used for that hybrid full duplex transmission.

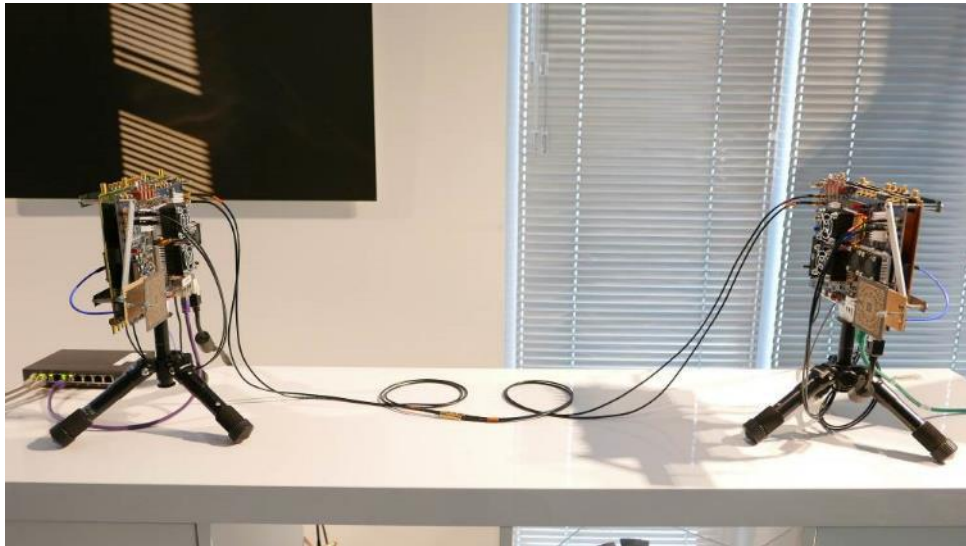


Figure 40: Two modem with 60GHz downlink and base band uplink

This set up allows validating some features like time and frequency synchronisation, mandatory for wireless transmission system. Nevertheless, the current radio modules introduce a heavy SNR degradation, and the received constellation illustrate the poor link quality. However, Figure 41 shows the achieved throughput is 330 Mbps for each user, which means an overall link capacity of 660 Mbps.

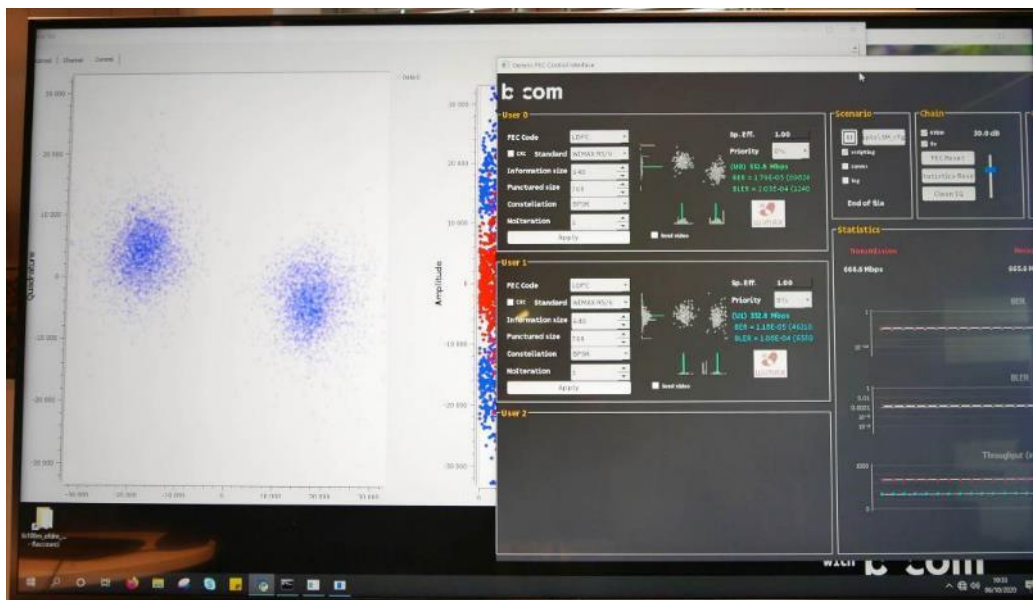


Figure 41: 60GHz receiver performances

4 Fibre Wireless Fiber PoC

This section introduces the FWF system, its current features and experimental results for its characterisation, Tbit/s data transmission and the transmission of VR content in real-time. The characterisation of the FWF terminals and the data transmission results have been published in international journal [4] and conference venues [5] [6].

4.1 Features

4.1.1 System Description

Figure 42 shows the system schematic and Table 11 lists the components of the FWF terminals. The communications signal, represented by yellow lines, is collimated out/into fibers with an optical collimator and steered using dual-axis steering mirrors. The red and blue lines represent the infrared localisation beacons provided by IR tags. The optical information signal and localisation beacon light are separated through the use of dichroic filters (DF1 & DF2). The localisation sub-system uses two board cameras, one for coarse tracking (CAM1 & CAM3) and second for fine tracking (CAM2 & CAM4). Further, use of optical band-pass filters (BF1 & BF2) minimises the possible interference to the localisation system from unwanted visible and infrared illumination sources.

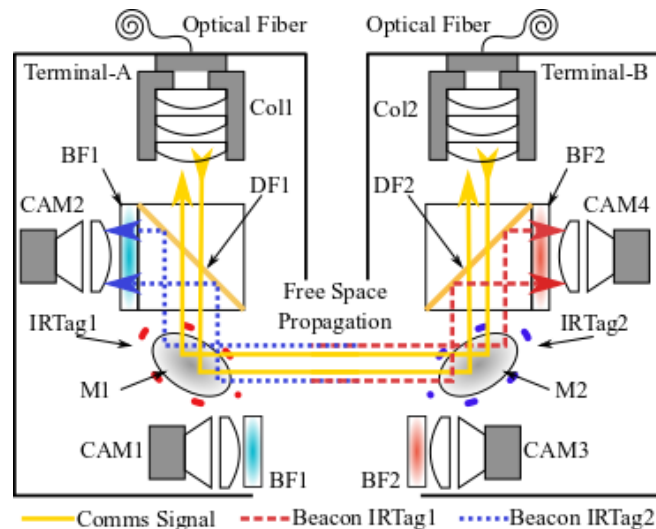


Figure 42: Block diagram of FWF system

The localisation sub-system uses two cameras to provide both wide FoV and higher accuracy. The wide FoV camera allows terminals to be located. The higher accuracy narrow FoV camera allows higher precision steering such that misalignment power loss is small. The gold-coated mirrors (M1 & M2) provide dual-axis beam steering with up to $\pm 50^\circ$ optical deflection per axis and a steering resolution less than $5 \mu\text{rad}$. The mirrors have a large angle step (20° step) response time of ~ 7.5 ms and a small angle step (0.1° step) response time of ~ 1.4 ms. These are sufficient for nomadic operations. It must be noted that the use of mirror based beam steering allows point-to-point links only. This means that access point can serve only one user at any one particular time. However, multi-user access can be supported by means of TDMA. Given the high data-rates that can be achieved (see Section 4.3), the TDMA approach with a short time-slot will be quite realistic and efficient to support multiple users through these terminals. Such a use case would also rely on RF based systems to provide reliable low-data rate connectivity (such as 60GHz RF wireless works together with WiFi).

Table 11: FWF Demonstrator Notation and Parameters

Notation	Details
BF1	Bandpass Filter-1, Central Wavelength 800 nm
BF2	Bandpass Filter-2, Central Wavelength 900 nm
Col1, Col2	Collimator-1 and Collimator-2
CAM1, CAM3	PixyCams with 50° horizontal and 30° vertical half Field-of-View (FoV)
CAM2, CAM4	PixyCams with 4° horizontal and 2.2° vertical half Field-of-View (FoV)
DF1,DF2	Dichroic Filter 1 and 2, cut-off at 900 nm
IRTag1	890 nm Infrared beacon for tracking
IRTag2	800 nm Infrared beacon for tracking
M1, M2	OptoTune mirrors for beam-steering

The coarse tracking cameras CAM1 and CAM3 were equipped with 2.1 mm focal length imaging lens (Edmund Optics 55-569) which resulted in a FoV of $\pm 50^\circ$ horizontally and $\pm 30^\circ$ vertically for the $3.89 \times 2.43 \mu\text{m}$ sensor fitted in the pixycam. This can be estimated using the following equation,

$$F(H, V) = 2 * \tan^{-1} \left(\frac{S(H, V)/2}{F_L} \right) \quad (4.1.1)$$

where $F(H, V)$ is the horizontal and vertical field of view (FoV), calculated from the lens focal length F_L and the width $S(H)$ and length $S(V)$ of the camera sensor, respectively. The pixycam sensor has 1280×800 pixels. However, the on-board post-processing results in 320×200 pixel frames at the I2C output. This gives approximately 0.3° per pixel resolution for the coarse tracking cameras. In order to choose the imaging lens for the fine tracking CAM2 and CAM4, the required pointing accuracy was investigated to ensure low loss coupling with fiber collimators. This involved measuring additional power loss due to misalignment when the transmitter is pointed at a static receiver, and the receiver pointed at a static transmitter, for a link distance of 3.5m. The results are shown in Figure 43. It can be seen that a $\pm 0.01^\circ$ misalignment in pointing results in an additional loss of approximately 3dB relative to maximum transmission. Therefore, a 50 mm focal length imaging lens (Edmund Optics 59-781) was used for fine tracking cameras, which resulted in a FoV of $\pm 2^\circ$ horizontally and $\pm 1.1^\circ$ vertically, leading to approximately 0.0125° per pixel resolution. The coarse and fine tracking camera imaging lenses have an entrance aperture of 17 mm and 27 mm, respectively.

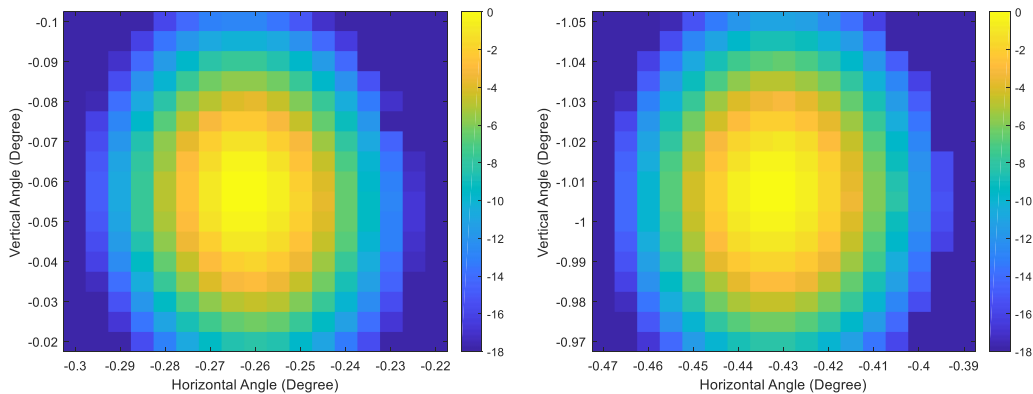


Figure 43: Additional loss (dB) due to pointing misalignment. Left hand figure shows transmitter pointing, receiver static. Right hand figure shows receiver pointing, transmitter static.

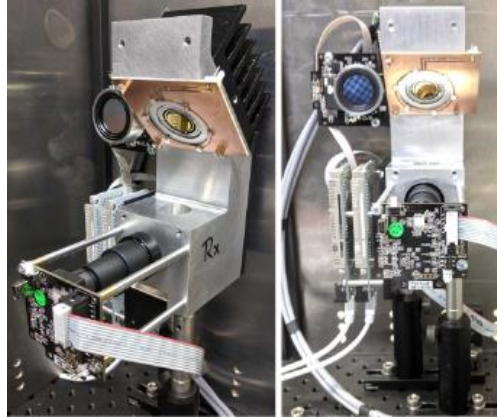


Figure 44: Assembled receiver (left) and transmitter (right) units.

Figure 44 shows the assembled units. The communication and localisation components are assembled with a metallic housing which is approximately $15 \times 14 \times 13$ cm. The IR tag PCBs are mounted on the same surface where the 2D steerable mirrors are affixed. Each PCB contains six IR LEDs forming a ring of 35 mm diameter, each LED separated by 17.5 mm. This enables the fine tracking camera to image a complete LED ring at a minimum link distance of 0.5 m and also resolve the 17.5 mm spatially separated LEDs at the opposite terminal for a link distance of up to 6 meters on bore sight. The IR LED ring is placed around the beam steering mirror so that the position of the centre of the mirror can be estimated. Figure 45 shows images of the IR beacon seen by a coarse and fine tracking camera, respectively at a link distance of 3.5 m. The IR beacon appears as a single source to the coarse tracking camera due to its wide FoV and the fine tracking camera is able to resolve the 17.5 mm spatially separated LEDs. The fine tracking cameras provide the position of each LED in a frame, from which an accurate position of the centre of the opposite IR ring or the opposite steering mirror is estimated. The measured optical power from the 810 nm and 890 nm LED rings, which use DC power supply, was approximately 0.43mW/cm^2 and 0.71mW/cm^2 at 100 mm distance. These power densities are within the Class-1 eye-safe limits estimated following the IEC60825-1 standard.

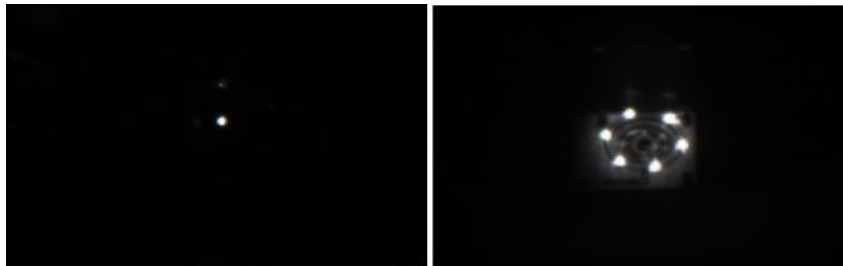


Figure 45: The IR beacon as seen by coarse (left) and fine (right) tracking cameras at 3 meter distance.

4.1.2 Terminal Control

The terminals can be controlled through a microcontroller or a PC. During the characterisation, terminals were controlled with a PC running MATLAB. The board cameras (Pixycams) stream object (IRTag) information in terms of its image size and centre on the sensor in pixels to Arduino Due boards at 50 frames per second (fps) rate via an I2C interface. This information is acquired by the controller PC connected to the Arduino boards via USB connection for further processing to obtain yaw and pitch angles for the beam-steering mirrors. Once the angles have been estimated, MATLAB commands are sent to the mirror driver boards (provided by OptoTune) via USB connection to tilt the mirrors for terminal alignment.

The terminals are aligned in a two-step localisation and steering procedure, which is illustrated by a flowchart shown in Figure 46. In the first step, the coarse tracking camera obtains rough positioning information of the opposite terminal. The coarse tracking positional information is converted to horizontal and vertical coarse link angles α_H and α_V , respectively, using (4.1.2), where $O_{CT}(H, V)$ represent the horizontal or vertical centre pixels of coarse tracking camera frames, $I_{CT}(H, V)$ is the horizontal or vertical pixel numbers representing the centre of the object's image in a frame acquired from the coarse tracking cameras, and $\delta_{CT}(H, V)$ is the measured

horizontal or vertical resolution of the coarse tracking cameras in degrees per pixel. The horizontal and vertical steering angles of the mirror at this point are given as $0.5\alpha_H$ and $0.5\alpha_V$, respectively.

$$\alpha(H, V) = \{O_{CT}(H, V) - I_{CT}(H, V)\} \delta_{CT}(H, V) \quad (4.1.2)$$

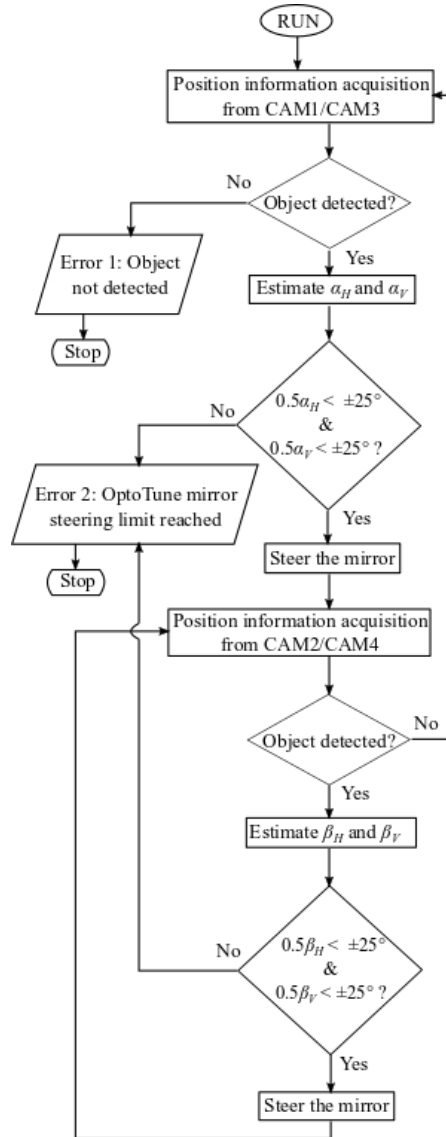


Figure 46: Localisation and steering process for terminal alignment.

The coarse alignment positions the tracked IR beacon into the FoV of the fine tracking cameras, which then estimates finer mirror steering angles. In this step, the coordinates of the six LEDs are obtained from the fine tracking camera at a 50 fps rate. Then, through the use of an elliptical fitting MATLAB function, the centre of the LED ring and hence the centre of the opposite mirror is estimated. The ring's centre coordinates are then converted to more precise link angles β_H and β_V , respectively, using (4.1.3), where $\theta(H, V)$ represents the horizontal or vertical alignment calibration coefficient. After fine tracking the horizontal and vertical steering angles of the mirror are given as $0.5\beta_H$ and $0.5\beta_V$, respectively. At this point the two terminals are aligned and up-link/down-link data transmission can take place.

$$\beta(H, V) = \{O_{FT}(H, V) - I_{FT}(H, V)\} \delta_{FT}(H, V) - \theta(H, V) \quad (4.1.3)$$

4.2 Characterisation of Localisation System: FoV, Link-Loss, Aberrations and Latency

4.2.1 System Setup

The FoV and link-loss evaluation was carried out using the experimental setup shown in Figure 47. The FWF terminals were placed on optical tables of same height. The free-space distance between the terminals was 3.5 m. One of the terminal was fixed to the optical table and the other terminal was rotated with the use of a rotation stage (driven by Newport ESP300). A 1550nm SFP+ transceiver module (Finisar FTLX1871M3BCL) was used as an optical source, which was driven by a bit error ratio tester (Spectronix Eye-BERT). A single mode fiber (SMF) connects the FWF terminals to SFP+ module and optical power meter (Newport 1919-R). A variable optical attenuator (VOA15-APC) was used between the BERT and transmitting terminal to control the output power.

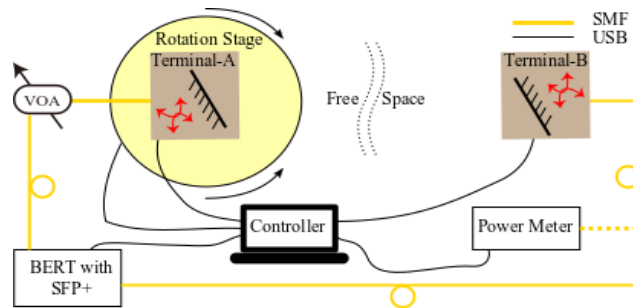


Figure 47: Experimental setup for FoV and aberration evaluation.

4.2.2 Field of View (FoV)

The FoV and operation of localisation and steering system was investigated by separate horizontal and vertical rotation of one terminal, while the other terminal remained static at approximately 0° steering angle. The transmit optical power was 0 dBm by default. Auto-alignment was performed using the localisation system and the received power (dBm) was recorded for every degree of terminal rotation both with and without the use of aberration correction. The results are shown in Figure 48 for both the terminals, which show that the bore-sight loss is approximately 7 dB, resulting from beam divergence, localisation limited beam steering accuracy and the collimation losses. In addition, aberrations in the localisation system lead to significant link loss as the link angle increases at any one terminal either in the horizontal or the vertical plane.

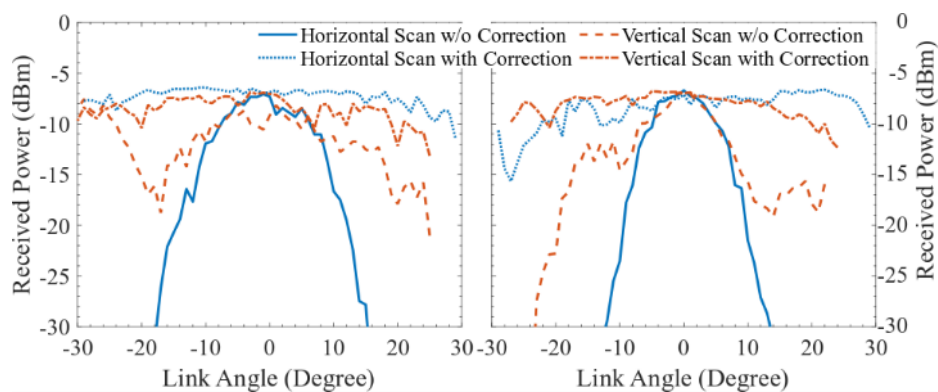


Figure 48: Link-loss (dB) vs link-angle for the two FWF terminals. The solid curves represent received power without aberration corrections and the dashed curves with aberration correction.

4.2.3 Aberrations and Calibration

The localisation error due to aberrations at each terminal were measured for different link angles in both horizontal and vertical steering axes, which are shown in Figure 49 in the form of steering angle correction for one of the terminals. The steering angle correction is measured by comparing the manual alignment angles with the automated alignment angles. These results show that the aberrations increase with increasing link angles, leading to positioning errors as high as 0.1° . The results also show that the steering in the horizontal and vertical planes is cross-coupled. These aberrations could potentially be generated by multiple factors, such as axial misalignment between mirror and the fine tracking camera, cross-coupling between the mirror rotation axis. It has not been possible to link these aberrations to one particular source. In this work, 2nd order polynomial equations of the form $\Delta\beta(H, V) = c_1\beta^2(H, V) + c_2\beta(H, V) + c_3$ were used to relate derived position from the localisation system and mirror steering angles to establish the link. The constants c_1 , c_2 and c_3 were obtained by applying a polynomial fit to the measured steering angle correction for every link angle. The results in Figure 48 show that the aberration correction significantly improves the received power and reduces the link loss by more than 20 dB for a link angle of $\pm 20^\circ$, which has been used as an example.

Although coarse tracking provides a FoV of $\pm 50^\circ$ horizontally and $\pm 30^\circ$ vertically, the FoV of the assembled terminals was limited to $\pm 29^\circ$ horizontally and $\pm 25^\circ$ vertically. The FoV in the horizontal plane was limited by the ellipticity of the IR Tags making it difficult for the fine tracking camera to resolve the elements of the LED rings for link angles greater than $\pm 29^\circ$ horizontally. The FoV in the vertical plane was limited due to the position of the fine tracking camera, which blocked the communication signal for link angles greater than $+25^\circ$ vertically. The location of the fine tracking camera can be changed to fully access the available coverage in vertical plane. In the horizontal plane the coverage may be enhanced by further improvements in the design of the localisation system and software.

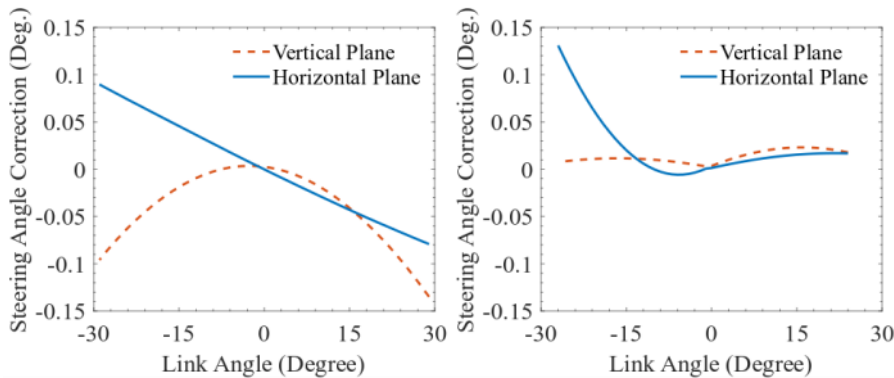


Figure 49: Steering angle correction (Degree) for one of the terminals for steering in horizontal plane (left) and vertical plane (right).

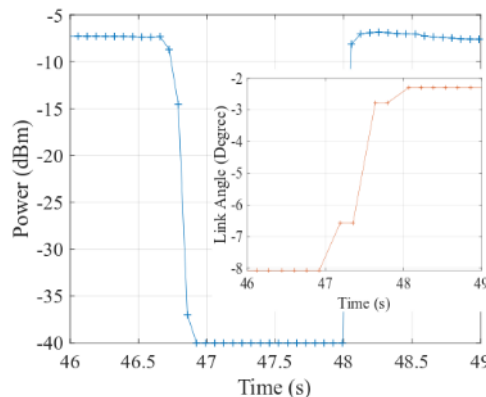


Figure 50: The time versus received power plot for the manual translation of the Terminal-B in lateral direction with respect to Terminal-A. The inset shows time versus link angle for the Terminal-B, to study the terminal tracking latency.

4.2.4 Tracking Latency Evaluation

The tracking latency was studied by manually translating Terminal-B in the lateral direction. The terminals continuously and independently tracked each other. The received power and link angle was monitored during the translation time. The received power was measured and recorded with a power meter, whereas the link-angle was estimated and recorded from the localisation & tracking system. The results are shown in Figure 50, which show that for one lateral translation of Terminal-B, the power is down for approximately 1.3 seconds (see main figure), during which the Terminal-B, as it is moved, tries to track Terminal-A six times (see inset), while the link angle changed from roughly -8 to -2.3 degree. This gives an average tracking time of 216 ms. Similar tracking behaviour and latency was observed on Terminal-A, as each terminal must track the other to maintain a link. The latency was further confirmed within the MATLAB by recording the time taken to run the coarse (~50 ms) and fine tracking codes (~150 ms). The measured characteristics of the FWF terminals are summarised in Table 12.

This latency is sufficiently low to support nomadic or quasi-stationary terminals. However, depending on the required level of mobility, this latency must be reduced. To do so a faster sensor or a different approach to tracking will be required. This is a subject of further research within the WORTECS project, with a second generation system under development.

Table 12: System features and specification.

Operating Field of View	+/- 25 degrees horizontally and vertically
Tracking system resolution (theoretical)	0.014 degrees horizontally and Vertically (corresponding to 1 camera pixel)
Tracking system resolution (measured)	0.021 degrees horizontally and 0.014 degrees Vertically (corresponding to 1 camera pixel)
Tracking system latency (measured)	216 ms (coarse and fine tracking combined)
Communications wavelength	1300-1600 nm (bidirectional)
Fibre input/output	SMF 28- APC connectors
Free space beam diameter	1.12 mm (theoretical) at Collimator output
Transmission power	Limited to <7dBm (Class 1 operation) by control of laser power
Tracking beacon wavelength	800 nm terminal A and 890 nm terminal B

4.3 Terabit/s FWF Transmission Results

In order to obtain results at Tb/s suitable data transmitters and receivers are required, and these are not available easily across the WORTECs project. An existing collaboration with the University of Southampton, under a UK funded project, allow us to undertake a joint experiment to demonstrate Tb/s capability.

Data transmission experiments in different positioning scenarios were conducted to experimentally verify the design of the presented FWF terminals, as illustrated in the layout shown in Figure 51. The location of beam-steering terminal-A was fixed on an optical bench and terminal-B, sitting on another optical bench, was moved along the lateral direction to four equally spaced locations. The vertical distance between the terminals was 3.5 metres. For every location of terminal-B, both of the mirror-based beam steering units had to adjust their steering angles to establish the fibre-wireless-link. Due to space limitations, experimental tests for the lateral displacement up to ~0.9 metres from the origin of the localisation FoV were performed. This results in a 2.54 m² full coverage, due to the symmetrical nature of the optical localisation system.

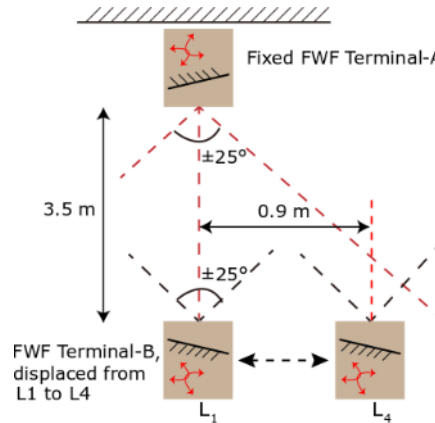


Figure 51: Experimental layout for testing 1 Tbit/s transmission over the FWF terminals.

Figure 52 shows the data transmission components. Ten standard ITU 100-GHz-spaced wavelengths from 1546.12 nm to 1553.33 nm were used as optical carriers to achieve the aggregate data rate of 1 Terabit/s. A Mach-Zehnder modulator driven by an arbitrary waveform generator (AWG) that generated 100 Gb/s Nyquist PAM-4 signals modulated each of the ten wavelengths. The odd and even WDM channels of the modulated optical signals were demultiplexed by a Finisar waveshaper and were de-correlated by using different fibre delays. They were then combined and amplified by a booster erbium-doped-fiber amplifier (EDFA). In order to ensure eye-safe operation, the output optical power at the transmitting end was set to 7 dBm (i.e. 3 dB below the eye-safety limit at 1550 nm as per the IEC60825-1 standard). At the receiving end, a pre-amplifying EDFA was employed and a tunable optical bandpass filter (OBPF) was used to individually select each of the WDM channels. The power of the received optical signal was varied by a variable optical attenuator before it was detected by the photodiode. The converted electrical signals were then captured by an 80 GS/s real-time oscilloscope and processed offline. A decision feedback equalizer (DFE) was used to recover the PAM-4 signals and the bit error ratios (BERs) were estimated via error counting.

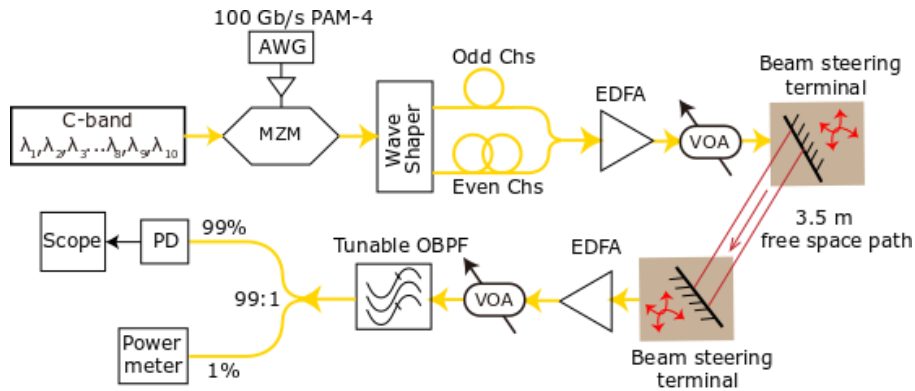


Figure 52: Experimental setup for testing 1 Tbit/s transmission over the FWF terminals.

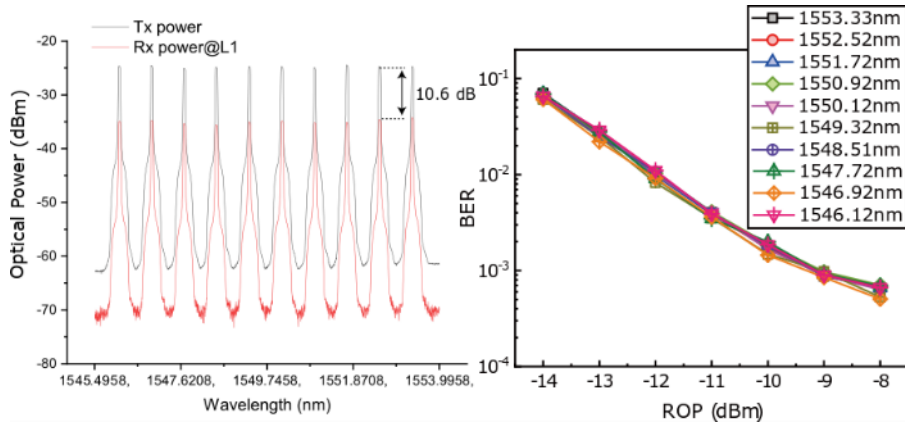


Figure 53: The transmitted and received optical spectra of the 10 WDM channels (left), measured BER curves versus received optical power (ROP) for all WDM channels (right) for optimal alignment at location L1.

The 3-dB bandwidth of the MZM and PD were around 20 GHz and 30 GHz, respectively. The passband bandwidth of the OBPF was 0.8 nm. Furthermore, the 7-dBm launched power corresponds to the total power of all ten WDM channels. Initial data transmission tests at the aggregate data rate of 1 Terabit/s were performed when FWF terminal-B was at location L1. In this case, terminals were close to boresight with almost no lateral displacement, as illustrated in Figure 51. The alignment of the indoor OWC link was manually optimized through 2D scans of both mirrors with a fine resolution of 0.01° to identify the minimum link loss. Figure 53 (left) shows the measured transmitted and received optical spectra of the 1 Terabit/s WDM signal. An optical link loss of ~10.6 dB was measured. Figure 53 (right) shows the measured BER curves versus received optical power for all WDM channels over the OWC link. A BER below the 7% forward-error-correction (FEC) threshold (3.8×10^{-3}) for all WDM channels was achieved. It can be seen that all the WDM channels of the OWC link have almost identical BER performance at all the received optical power values. This is due to the wavelength transparent nature of the mirror-based beam steering terminals.

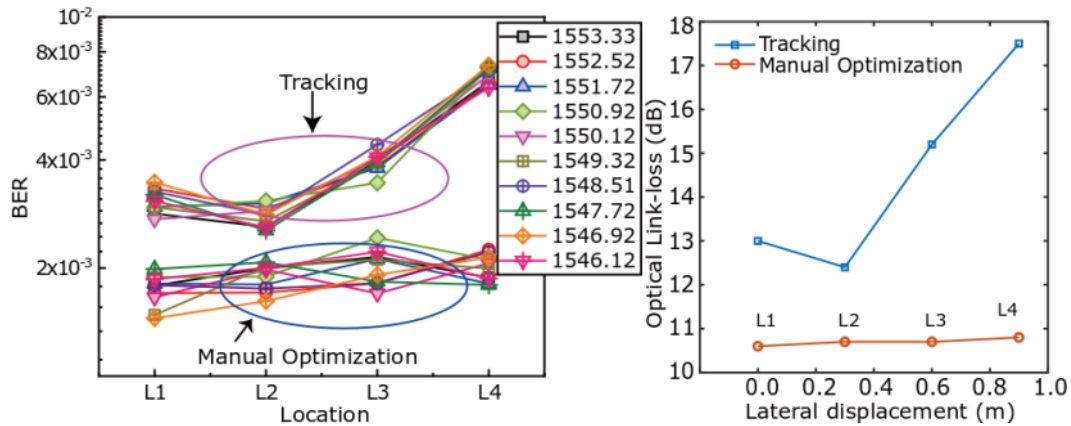


Figure 54: At the four discrete locations, for both OWC links established by the tracking system and manually optimized OWC links, (left) BER curves of all WDM channels at -10 dBm received optical power, and (right) corresponding optical link loss.

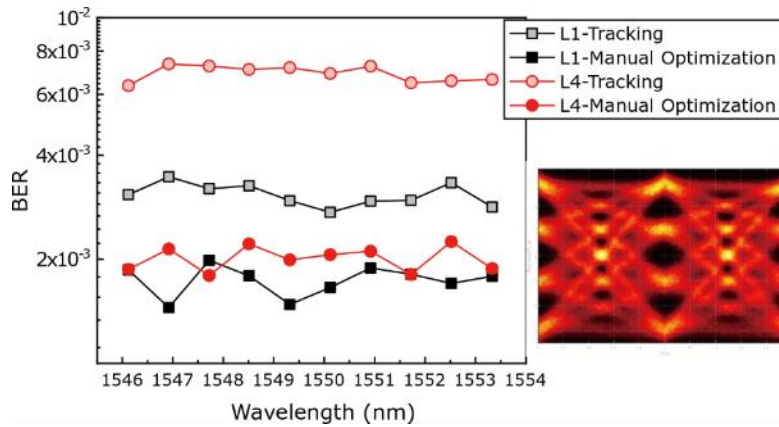


Figure 55: BER curves (left) of all the WDM channels at location L1 and location L4 for both tracking established OWC links and manually optimized OWC links at -10 dBm received optical power. A typical 100 Gb/s PAM-4 eye diagram (Right) at -9 dBm ROP for the manually optimised OWC link at location 1.

To further investigate the indoor OWC system under tracking and localization, mirror terminal B was moved between four discrete locations, as illustrated in Figure 51. At each location, OWC links were first established by the localisation system and were subsequently manually optimized. For each case of the tracked and optimised alignment, optical link loss was measured and the BERs for each of the ten PAM-4 WDM transmissions were evaluated. Figure 54 (left) shows the BER measurements at -10 dBm received optical power for all WDM channels on both localisation established links and further manually optimized links. Figure 54 (right) shows the measured optical losses for both the tracked links and optimized links at each location. It is observed that the optimal alignment with manual steering provides better BER than the auto-alignment, especially as the lateral distance increases. This is due to the 0.01° difference between the steering accuracy of the localisation and optimal alignment scenarios. However, it must be noted that the manual alignment is time consuming in comparison to tracked alignment. Further optimisation of the tracking system could potentially overcome this additional power loss. More discussion on this is presented in the next section.

Figure 55 compares the BER at -10 dBm received optical power versus wavelengths of all WDM channels for both the localisation established links and manually optimized links respectively at location L1 and location L4. It indicates that the data transmission performance of different WDM channels is similar at each position and wavelength. A typical PAM-4 eye diagram at 100 Gbit/s is also shown in Figure 55.

4.4 Real-time Transmission of VR Content

A 10G SFP+ transceiver module (FTLX1871M3BCL) which provides 0 dBm output power at the transmitter was used for real-time data transmission experiments. The receiver sensitivity was determined using a free-space 10.3 Gbit/s data transmission link between terminals 3.5m apart. The transmit power was reduced through the use of a VOA (VOA15-APC), leading to reduction in the received power and degradation of BER. A plot of BER vs received power is shown in Figure 56. It can be seen that the receiver has a sensitivity of -27 dBm for a BER of approximately 10^{-9} , giving a link budget of 27 dB with a 0 dBm transmission power.

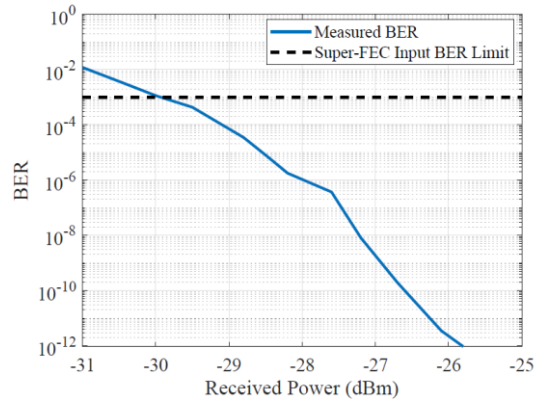


Figure 56: BER performance of FTLX1871M3BCL SFP+ module for a 10.3 Gbit/s free-space transmission.

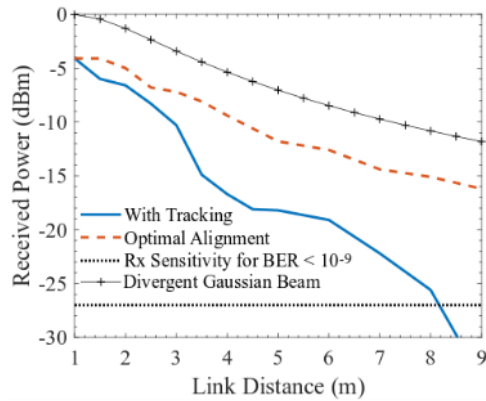


Figure 57: Bore sight communication range of FWF terminals with SFP+ based 10.3 Gbit/s free-space transmission.

The terminals were placed on separate trolleys at roughly 1 m height and the distance between the terminals was increased and data transmission was established through tracking for different link distances. The link distance vs received power results are shown in Figure 57. It can be seen that the localisation system can provide bore-sight coverage of up to 8 m with a link margin of at least 1 dB, maintaining 10.3 Gbit/s transmission. The link-loss increases with the link distance partly due to beam divergence and the limited accuracy of localisation system. Given that optical power can be increased to 10 dBm at the transmitter (i.e. to the eye-safety limit), beyond 8 m transmission can be established by means of optical amplification, which can also be used at the receiver side to further increase the link-budget. Figure 57 also shows the received power vs link distance curve for optimally aligned terminals. The results show that the optimal alignment can reduce the link losses by up to 10 dB for a link distance of 8 m and can further increase link distance significantly. However, as previously mentioned the optimal alignment with manual 2D scanning of the steering mirrors is impractical due to time inefficiency. Operation of a 1310 nm transmission was also investigated using another SFP+ transceiver, where an extra 2 dB loss was observed for this shorter wavelength optical signal.

$$P_r = P_t - L_{Gauss} - L_{Fix} - L_{Align}$$

$$L_{Gauss} = P_t e^{\frac{-2R_r^2}{\omega_L^2}}$$

$$\omega_L = \omega_o \sqrt{1 + \left(\frac{L}{z_o}\right)^2} \quad (4.1.3)$$

$$z_o = \frac{\pi \omega_o^2}{\lambda}$$

Figure 57 also shows a theoretical curve of the received power for a divergent Gaussian beam, estimated using the above set of equations (4.1.4), assuming that $L_{Fix} = 0$ and $L_{Align} = 0$, where, P_r is the received power, P_t is the transmit power, L_{Gauss} is the free space loss of a divergent Gaussian beam, L_{Align} is the link misalignment loss, R_r is the receiver aperture radius, ω_L is the beam waist as a function of link distance L , ω_o is the e-1 beam waist at the transmitter aperture, and z_o is the Rayleigh range.

The collimator (TC06-1550) used within terminals has a full angle divergence of 0.101° and e⁻¹ beam waist of 0.82 mm. Comparing the theoretical received power with that of optimally aligned curve, it can be seen that there is 4 dB additional fixed loss (L_{Fix}) in the FWF system. A small portion of this fixed loss comes from collimation and the rest comes from fiber connectors, etc. Overall the trend of the theoretical and optimally aligned received power curves is similar, while the tracked system has additional misalignment loss (L_{Align}) leading to more losses as the link distance increases.

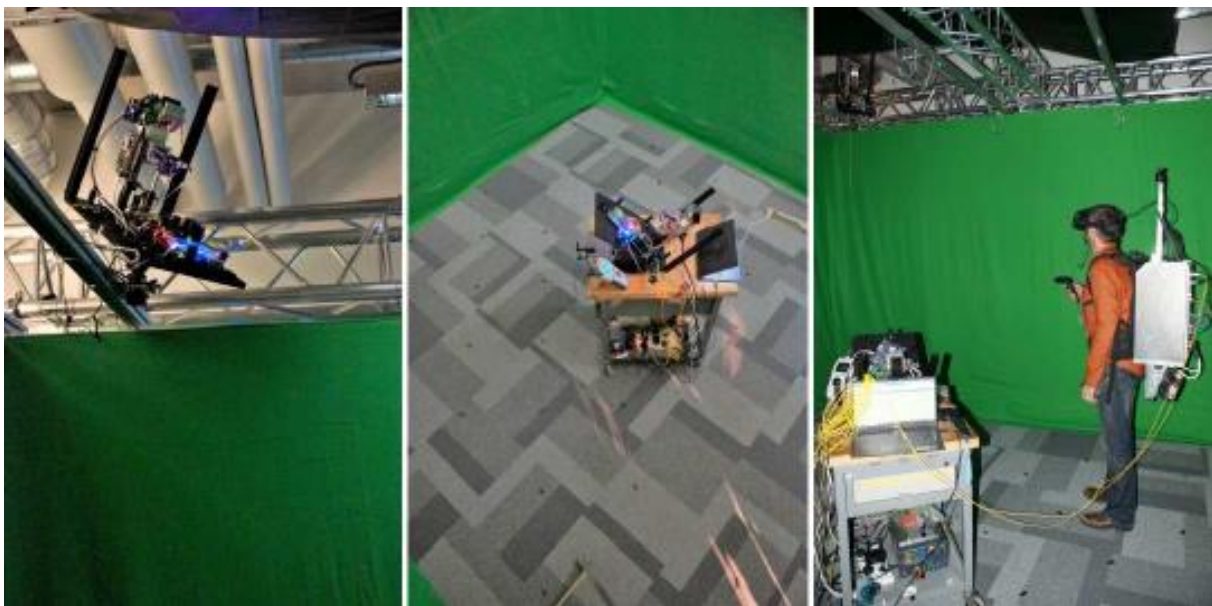


Figure 58: FWF terminal setup in 4 x 4 x 3 meter indoor testing facility at BCOM laboratory. The AP terminal in one corner at 3.5m height (left), the UE terminal on the room floor (centre) and VR-HMD connected to the UE terminal (right).

The terminal coverage was evaluated in a $4 \times 4 \times 3$ meter indoor testing facility at the BCOM laboratory in Rennes, France. Figure 58 shows the setup of terminals within the test facility. One terminal acted as access point (AP), mounted in one corner of the room at a height of 3.5 m. The other terminal acted as user-equipment (UE), which was placed on a trolley (roughly 1.15 m from the floor) so that it could be moved across the room to study achievable coverage with the 10G SFP+ transceivers.

Both up-link (UL) and down-link (DL) 10.3 Gbit/s data transmissions were performed and the terminals were aligned using the localisation system for each location of UE. The received power was measured at each terminal when the UE moved to different locations. The results are shown in Figure 59, which reveal that the localisation system can provide approximately 4.9 m^2 coverage within the $4 \times 4 \times 3$ meter room, beyond which the localisation system is unable to work due to its limited FoV. Additionally, the 10 Gbit/s UL and DL transmissions, with limited 27 dB link budget, worked well within 3.14 m^2 with a BER $< 10^{-9}$.

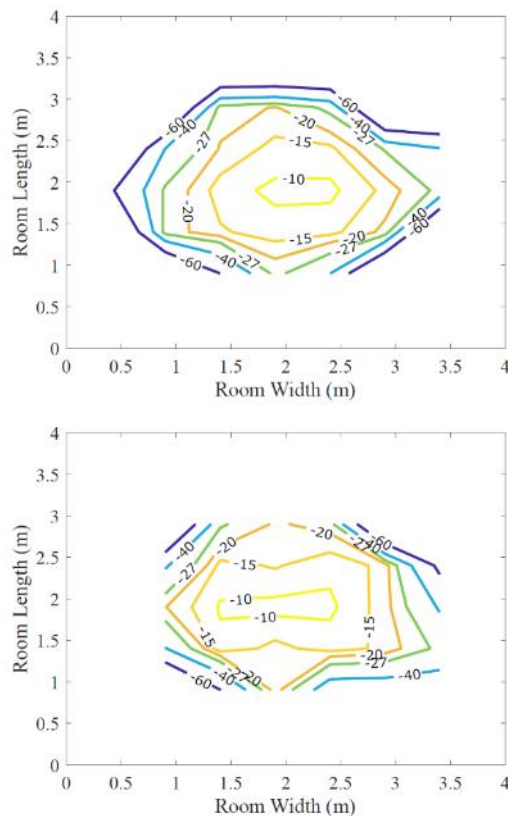


Figure 59: FWF terminal down-link (top) and up-link (bottom) received power levels (dBm) for 10.3 Gbit/s free-space transmission when the UE terminal moved across the room floor.

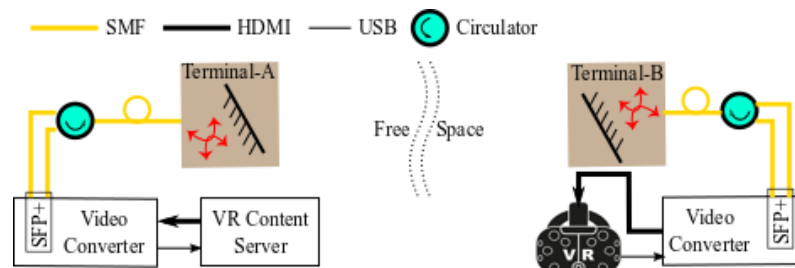


Figure 60: Experimental setup for data transmission using VR content.

In addition to this, a full-duplex transmission was performed using virtual reality (VR) content. The experimental diagram is shown in Figure 60. The goal was to use a classical VR set up with a wireless link from the VR server to the VR head-mounted display (VR-HMD). The DL carried VR content from the VR server to the VR-HMD. A home-made application named “Virtual Arctic Expedition”, which provides a visit to sea spaces via virtual diving was used as VR content. On the AP side, a VR server (based on Core i7 PCU + GPU GTX980i) provided this video content as a HDMI signal, with a resolution of 2160 x 1200 pixels at 90Hz using 8 bits per pixel. The video signal had a raw throughput of 5.6 Gbps, which fed a video converter (ArriaX FPGA) via its HDMI input port. The video converter converted the HDMI signal into data flow using 10GETH protocol, which fed an SFP+ transceiver (FTLX1871M3BCL). This SFP+ transceiver was connected to the AP (Terminal-A) via SMF and a circulator (ThorLabs 6015-3-APC) to enable full-duplex communication.

On the UE side, the user terminal (Terminal-B) was connected to another video converter board via SMF and a circulator, where the received Ethernet packets were converted back into the HDMI video signal. This signal was then streamed to a VR-HMD (HTC Vive) connected to the video converter via an HDMI cable. The UL was required to carry the localisation information to the video server from the VR-HMD using the same video converters and optical SFP+ transceivers. The VR-HMD transfers the localisation information to the video converter via a USB link and on the AP side another USB link is used to transfer this information from the video

converter to the VR server. Therefore, in the full duplex optical link, the DL carried the video content (5.6 Gbps) and the UL carried the localisation information (several Mbps). This localisation information is specifically needed for the VR-HMD, generated by the LightHouse system provided with the HTC Vive and it should not be confused with the localisation and tracking system information for beam-steering in the terminals. The video transmission was tested over different locations within the test facility and no disruption was observed. However, use of additional components (two circulators and four FC/FC connectors) for full-duplex wireless operation introduced approximately 5dB additional loss in the UL and DL, which limited the coverage to 1.5 m² for video transmission.

It is apparent that the data/video transmission coverage can be further increased to 4.9 m² by increasing the transmit power to the Class-I eye-safety limit and by using optical amplification at the receiver of each terminal. In addition to this, there are several ways to further optimise or improve the performance of the tracking and beam-steering system to minimise the pointing loss. The pointing error is measured by comparing the pointing angles obtained from the localisation & tracking system to those obtained from optimal alignment. The implemented pointing correction uses the pointing error information obtained from one-dimensional rotation/steering in the horizontal and vertical planes. This one dimensional aberration correction in horizontal and vertical plane (as shown in Figure 48), minimises the pointing loss very effectively in the respective planes, to close to the values obtained by manually optimised pointing. However, the link losses observed in a two-dimensional steering increase significantly in the available FoV as the link angle increases, as seen in Figure 59. Similar conclusions can be made from the results in Figure 54, which shows that manual optimisation provides better BER. This indicates that the horizontal and vertical corrections are not separable, so a full two-dimensional correction mapping is required to obtain similar losses to those achieved using manual optimisation. In addition to this, the OptoTune mirror used in the FWF terminals can be steered with a pointing accuracy of 0.001°. This was verified experimentally where a smaller pointing loss was observed by manually aligning the terminals with such accuracy. However, the measured accuracy of the tracking system is 0.02°. Therefore, there is a room for further improvement in the tracking system performance, which can further minimise the pointing loss. A position sensitive detector (rather than a camera) is currently being evaluated as a fine-tracking sensor (which also offers lower latency), and a higher pixel-count camera may also offer a route to higher accuracy.

As part of the WORTECS project, the UOXF partner is currently working on the development of generation-II of these FWF terminals to minimise the tracking latency and further improve the tracking accuracy and overall coverage. Details of this ongoing work will be presented in the deliverable D4.7.

5 Propagation Model

The propagation of electromagnetic waves whose wavelength is comparable (or smaller) to the elements that comprise the scenario can be assumed to follow a ray-based behaviour. In indoor scenarios, the associated frequency lower bound is located around 60 GHz. The ray approximation has several implications. On the one hand, all the emitted energy can be approximated by an infinite sum of infinitesimal rays (energy carried by the smallest possible solid angle). On the other hand, each one of the rays that compose the emission are independent. Nonetheless, in practical implementations, the infinite summation is usually substituted by a finite aggregation of rays carrying the whole emitted power.

When the channel impulse response of a link is of interest, Monte Carlo integration schemes are the most extensively used technique for wavelengths in the aforementioned range (60 GHz and beyond). This family of techniques is based on a simple set of equations governing emission, reflections, and reception. The performance of Monte Carlo schemes depends on the statistical assumptions made on the propagation. The first Monte Carlo Ray Tracing (MCRT) schemes used in Optical Wireless Communication (OWC) calculated random ray bounces until, by pure luck, a ray strikes the receiver. This first approximation, although accurate, shows unacceptable convergence times. A Modified MCRT (MMCRT) in which “forced” contributions were calculated on each rebound sped up the convergence by several orders of magnitude, diminishing the number of rays needed.

This chapter is focused on presenting the simulation environment developed for the WORTECS project. The simulation algorithm has been generalized for any kind of electromagnetic wave, taking into account both RF and Intensity Modulated with Direct Detection (IMDD) systems. However, since experimental characterizations of channel impulse responses are difficult to find in the literature for the RF-band, this part stills need validation. Moreover, the behaviour of beyond-60-GHz RF reflections is also a topic that need more investigation.

5.1 High level simulation model

The developed simulator has been designed targeting the highest level of flexibility and portability. It has been developed using Python, since it is an interpreted programming language (portable), and under the Object Oriented Programming (OOP) paradigm to provide scalability and a modular approach. Although the simulator has been already presented in other deliverables, a brief summary is being presented in order to keep the readability.

The simulator has been divided into three main parts: pre-processing, MMCRT, and post-processing. During the pre-processing stage, an OCTREE structure is inflated using a triangularized mesh file (in .obj format) with the geometry of the scenario. This structure, which has been recently introduced into the simulator, enhances impact calculation performance, since it implements a logarithmic complexity search algorithm. The MMCRT stage carries out the Monte Carlo integration scheme using a modified version of the algorithm. In this part, several sub-schemes have been tested. The MMCRT algorithm can be implemented taking into account the radiation pattern of the emitter, carrying out emphasized sampling. However, this emphasis does not allow the use of other strategies that may provide higher flexibility, and a uniformly-sampled scheme in which the light path of each arriving ray is stored has been also tested. This approach, although it is more memory-consuming and time-consuming, provides improved flexibility, which can be used during the last stage of the algorithm. This last stage, the post-processing stage, takes advantage of the way the information has been stored. In the basic approach, the arrival angles, flight time, and power of each ray is stored for each receiver point. Using this information, it is straightforward to project the n-dimensional vectors into a time-power signal (the impulse response), using receiver parameters such as active area, field of view and attitude. Furthermore, if the light-path were stored and hence a light footprint could be obtained, testing different surface materials, reflection patterns and transmitter radiation patterns would be simple. In this recently proposed approach, each ray carries not only information about incidence angle, power (only due to geometry and not due to reflections) and flight time, but

also information about the impact and output angles on each rebound, and the material of each impact surface. As in the other scheme, the resulting tensor can be projected using the appropriate information.

5.2 Mathematical description of the simulation model

This subsection describes the mathematical formulation of the simulator. Some emphasis will be put on the ray generation procedure and the post-processing stage. Ray generation is one of the most time-consuming operations in MCRT algorithms. In general terms, if no emphasized sampling is considered, ray generation can be carried out as Equation 5.2.1 describes.

$$\begin{aligned}\theta &\sim U\left(0, \frac{\pi}{2}\right) \\ \varphi &\sim U(0, 2\pi)\end{aligned}\quad (5.2.1)$$

Where θ is elevation, φ is azimuth and $U(a, b)$ is a uniform distribution between a and b . This sampling scheme does not take into account any privileged direction, and fits an hemispherical radiation. On the other hand, if any radiation pattern $R(\theta)$ (with revolution symmetry) were targeted, the ray generation procedure should take into account the mentioned privileged directions. Equations 5.2.2 and 5.2.3 illustrate the procedure.

$$f_{\theta}(\theta) = R(\theta) \cdot \left(\int_{\theta} R(\theta) d\theta \right)^{-1} \quad (5.2.2)$$

The probability density function (PDF) of the generated rays is associated to the radiation pattern, complying with Kolmogorov's axioms. In order to generate rays following $f_{\theta}(\theta)$, the inverse function of its integral must be calculated.

$$\begin{aligned}\theta &= F^{-1}(r) \\ \varphi &\sim U(0, 2\pi)\end{aligned}\quad (5.2.3)$$

F is the distribution function (integral of the PDF) or cumulative distribution function, and r is a uniform random number between 0 and 1 (range of a PDF). Nonetheless, F has not usually a tractable closed-form expression, and this procedure must be carried out numerically.

Once a ray is generated and its impact within the scenario calculated, the resulting point behaves as a new emitter, whose output power must be splitted in a finite number of rays as occurs with the transmitter. Hence, the aforementioned procedure can be applied again after each rebound.

The mathematical expression of the resulting impulse response using MMCRT can be observed in Equation 5.2.4. This equation is general, but some of its parameters will take a value or other depending on the geometry.

$$h(t, \vec{r}, \hat{v}) = h_{LOS}(t, \vec{r}, \hat{v}) + \frac{P_{tx}}{N} \sum_{i=1}^M \delta(t - t_i) \prod_{j=1}^{k(i)} L_j \quad (5.2.4)$$

$h(t, \vec{r}, \hat{v})$ is the impulse response at point \vec{r} and incidence angles \hat{v} . $h_{LOS}(t, \vec{r}, \hat{v})$ is the LOS part of the impulse response. N is the number of generated rays at the transmitter. $\delta(t - t_i)$ is a Dirac's delta at time t_i , which corresponds to the delay of the i -th arriving ray (out of the total M arriving rays). $k(i)$ is the amount of rebounds of the i -th ray prior to impacting with the receiver. Finally, L_j is the power loss at the j -th rebound of the i -th ray. The form of L_j depends on the impact angle at each surface, the output angle, the type of material, etc. Generally, L_j is calculated as Equation 5.2.5 shows.

$$L_j = L_j^{(geom)} L_j^{(phys)} L_j^{(scat)} \quad (5.2.5)$$

$$\begin{aligned}
L_j^{(geom)} &= \frac{1}{d_j^2} (\hat{n}_j, \hat{v}_j) \\
L_j^{(phys)} &= \rho_j \\
L_j^{(scat)} &= \frac{1}{K} R_j(\hat{v}_{j+1})
\end{aligned}$$

The power loss after a rebound can be divided into three parts. The geometrical loss $L_j^{(geom)}$ depends on the sub-link range d_j , the surface's normal vector and the ray direction. The physical loss is mainly described by the reflectivity of the material ρ_j . Finally, the loss due to light scattering (diffuse reflection) depends on the number of generated rays, the reflection pattern and the output angle. It must be noted that depending on the sampling scheme, $L_j^{(scat)}$ may take into account the reflection pattern or not (emphasized sampling does not need it).

Once the MMCRT simulation has finished, the resulting information must be projected into a time-power vector in order to have a real estimation of the impulse response. This is carried out during the post-processing stage using Equation 5.2.6.

$$h(t) = A_{pd} G_{lens} h(t, \vec{r}, \hat{v}) \cdot \hat{n}_{rx} \Theta \left(h(t, \vec{r}, \hat{v}) \cdot \hat{n}_{rx} - \frac{FOV}{2} \right) \quad (5.2.6)$$

A_{pd} is the photodetector area, G_{lens} is the lens gain, \hat{n}_{rx} is the receiver's normal vector, Θ is Heaviside's theta function, and FOV is the field of view of the receiver optics, which is related to the lens gain assuming the use of a CPC (Equation 5.2.7).

$$G_{lens} = \left(\frac{n_{mat}}{\sin \left(\frac{FOV}{2} \right)} \right)^2 \quad (5.2.7)$$

Where n_{mat} is the refractive index of the CPC material (Typically an index of 1.45 for PMMA is used).

5.3 Design of the Software as a Service platform

The WORTECS simulation model has been developed into a Software as a Service (SaaS) platform. The main objective of this platform is to provide an easy interface for OWC link designers. The designed platform comprises the following elements.

- **Python-based simulator.** This part needed some adaptation for supporting JSON-based configurable calls and for providing a serializable output.
- **API endpoint.** This is the main connection between users and the simulator itself. This API currently provides scenario upload and simulation operations. In the next future, user support and security will be implemented.
- **Database for materials and scenarios.** This database is required to store information about the materials and their corresponding reflection patterns.
- **Web interface.** An easy web interface using the Model View Controller (MVC) paradigm has been developed to show the simulator capabilities.

Figure 61 depicts the block diagram of WORTECS SaaS.

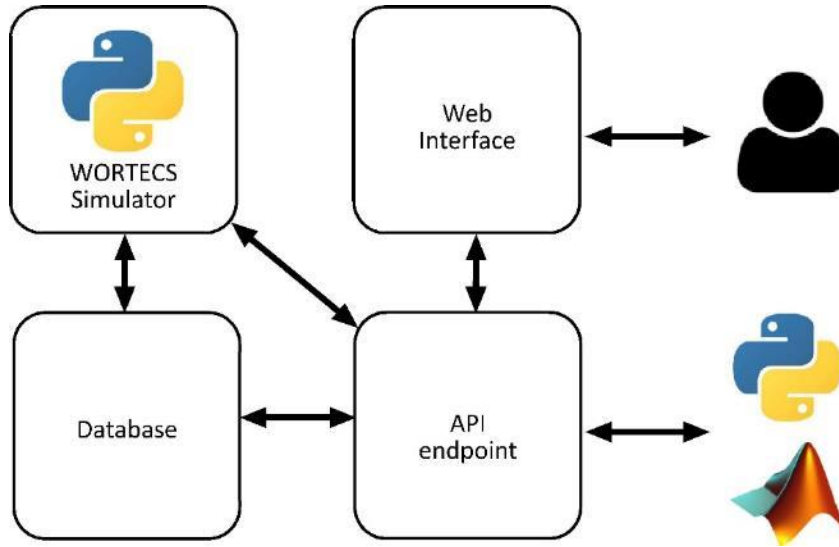


Figure 61: WORTECS Software as a Service architecture.

The API endpoint has been designed following the Create Read Update Delete (CRUD) paradigm, including the following directives (Table 13).

Table 13: Parameters of WORTECS SaaS API endpoint.

Directive	Parameters	Action
scenario	<ul style="list-style-type: none"> • id. The ID number of the scenario. • file. A container used in POST requests to upload a scenario file. 	<ul style="list-style-type: none"> • GET. Without parameters lists all the available scenarios. Including the id selects the corresponding scenario to carry out simulations and returns metadata. • POST. Uploads a new scenario using the file parameter. The new scenario is select as target scenario by default.
receiver	<ul style="list-style-type: none"> • height. Sets the receiver plane height for the next simulation. • number. Sets the number of uniformly-distributed receivers for the next simulation. 	<ul style="list-style-type: none"> • GET. Without parameters retrieves the current height and number configuration. It ignores any parameter included in the request. • POST. Sets height and/or number.
queue	<ul style="list-style-type: none"> • rays. Sets the number of generated rays (default is 10000). • format. Decides the output format between JSON or CSV (default is JSON). 	<ul style="list-style-type: none"> • POST. It only supports POST requests. Since the simulation takes a while, this request returns directly if the simulation has been queued correctly or not, returning the simulation ID (sid).
simulation	<ul style="list-style-type: none"> • sid. The simulation ID. 	<ul style="list-style-type: none"> • GET. It only supports GET requests. If no parameter is indicated, it returns a list of simulations with their status (queued, simulating, finished, error). If sid is included, it returns the simulation status, and if it is finished, it also returns the output structure.

The platform provides two possibilities, direct connection using the API endpoint or web interface. The web interface targets users without programming skills, or users that want to easily test simple scenarios. On the other hand, the API endpoint provides several useful directives that enable a more comprehensive control of the scenarios.

The development of both API and web interface is currently 80% complete, and more testing is needed to ensure smooth and error-free execution. An example screenshot of the web interface can be seen in Figure 62. This interface was developed using the Express library of Node.js and Material.

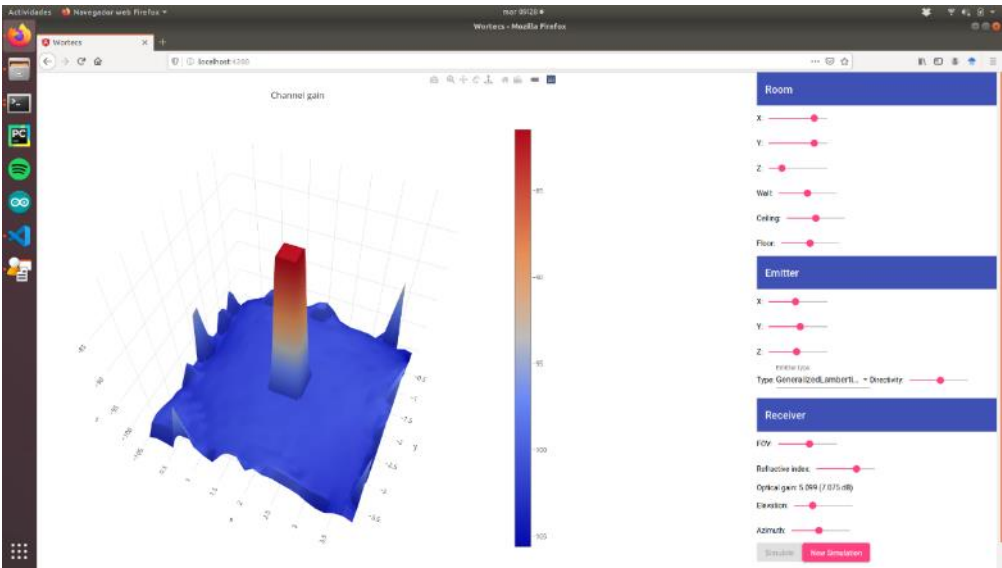


Figure 62: Web interface for WORTECS SaaS.

6 Conclusions

This deliverable presented different PoCs for indoor OWC developed in the H2020 project WORTECS. The broad and narrow beam optical link approaches were explored to develop Gbps and Tbps solutions, respectively, at the *last few meters*.

The OWC PoC (PoC 3) relies on the use of ITU-T G.hn standard chip for the design of the digital board. Two different digital boards (each by partner PLF and OLD) were developed and the performance of each board was evaluated to ensure Gbps capability. The design for the analog and optical front-end boards for PoC 3 was presented and their communication capabilities were specified, and these have been evaluated through initial laboratory testing. The investigation into the design of two different receivers based on PD and APD was also discussed and their communication capabilities were compared.

The design of a hybrid RF and optical wireless communication system (PoC 7) was also described in this deliverable. The design of a digital board, which is capable to process multiple baseband signals at the same time was discussed in detail and the designs of analog board, which acts as an interface between the digital board and the air-interface systems, was also presented. Designs of three different front-ends at i) 28 GHz, ii) 60 GHz and iii) Optical Infrared signals has been presented along with description of some initial tests on the digital board. Given the front-end boards are still under development, the performance evaluation of this PoC cannot be provided in this deliverable.

The design, implementation and performance evaluation of FWF PoC (PoC 6) for OWC with realistic communication and localisation coverage was also presented. This PoC focused on a small form factor design of beam-steering and tracking terminals to steer the light out of a fiber optic in free space at one end and guide it back into a fiber optic at the other end. The FWF PoC achieves a 50° full-angle FoV with an accuracy of 0.02° and a tracking latency of approximately 200ms. This has been achieved using dual-axis fast steering mirrors and small form factor low-cost, low pixel-count cameras. Through laboratory based experiments, a 1 Tbit/s transmission capability has been demonstrated. Considering a room size environment, 4.9m^2 localisation coverage has been achieved. Further, using off-the-shelf SFP+ modules, a 10 Gbit/s link between access and user terminals was demonstrated over a 3.14m^2 coverage area. A full-duplex wireless link between a VR server and a VR-HMD using the FWF terminals was also demonstrated, where VR content was streamed to VR-HMD and HMD related localisation information was streamed to VR server in real-time. The ongoing work related to FWF research is focused on increasing the tracking speed to enable terminal mobility.

Finally, this deliverable presented a channel simulation tool, which models wireless propagation channel for beyond 60 GHz RF and optical spectrum. The details of the GUI design and the mathematical model were presented and discussed in detail. This tool is expected to be made available for the wireless communication research community.

7 References

- [1] ITU, "G.9960 : Unified high-speed wireline-based home networking transceivers - System architecture and physical layer specification," [Online]. Available: <https://www.itu.int/rec/T-REC-G.9960-201811-I/en>.
- [2] MaxLinear, "88LX5152 and 88LX5153 Data Sheet Wave-2 G.hn Digital Baseband (DBB) Processor," [Online]. Available: https://www.maxlinear.com/ds/88lx5152_88lx5153.pdf. [Accessed Aug 2020].
- [3] MaxLinear, "88LX2730 Data Sheet Wave-2 G.gn AFE," [Online]. Available: <https://www.maxlinear.com/ds/88lx2730.pdf>. [Accessed Aug 2020].
- [4] R. Singh, F. Feng, H. Yang, F. Grahame, D. Rushikesh, V. Guillaume, B. Olivier, P. Periklis and O. Dominic, "Design and Characterisation of Terabit/s Capable Compact Localisation and Beam-steering Terminals for Fiber-Wireless-Fiber Links," *IEEE Journal of Lightwave Technology*, 2020.
- [5] Y. Hong, F. Feng, B. Kyle, T. Natsupa, S. Ravinder, F. Grahame, O. Dominic and P. and Periklis, "Beyond Terabit/s WDM Optical Wireless Transmission using Wavelength-Transparent Beam Tracking and Steering," in *Optical Fiber Communications Conference and Exhibition (OFC)*, 2020.
- [6] S. R, S. A, F. G and O. D, "Fiber-wireless-fiber terminals for optical wireless communication over multiple bands," in *IEEE Photonics Conference*, 2020.
- [7] A. Stimming, P. Giard and A. Burg, "Comparison of Polar Decoders with Existing Low-Density Parity-Check and Turbo Decoders," in *IEEE Wireless Communications and Networking Conference Workshops (WCNCW)*, San Francisco, CA, 2017.
- [8] A. Li, L. Xiang, T. Chen, R. Maunder, B. Al-Hashimi and L. Hanzo, "VLSI Implementation of Fully Parallel LTE Turbo Decoders," in *IEEE Access*, 2016.
- [9] B. Tahir, S. Schwarz and M. Rupp, "BER comparison between Convolutional, Turbo, LDPC, and Polar codes," in *2017 24th International Conference on Telecommunications (ICT)*, Limassol, 2017.
- [10] T. Mohsnein, D. Truong and B. Baas, "Low-Complexity Message-Passing Algorithm for Reduced Routing Congestion in LDPC Decoders," in *IEEE Transactions on Circuits and Systems*, 2010.
- [11] J. Lopez-Hernandez, R. Perez-Jimenez and A. Santamaria, "Modified Monte Carlo scheme for high-efficiency simulation of the impulse response on diffuse IR wireless indoor channels," in *Electronics Letters*, vol. 34, no. 19, pp. 1819-1820, 1998.
- [12] D. O'Brien and al, "High-Speed Optical Wireless Demonstrators: Conclusions and Future Directions," *Journal of Lightwave Technology*, vol. 30, no. 13, pp. 2181-2187, 2012.
- [13] S. Dissanayake and et. al, "Comparison of ACO-OFDM, DCO-OFDM and ADO-OFDM in IM/DD Systems," *Journal of Lightwave Technology*, vol. 31, no. 7, 2013.
- [14] D. Barros and et. al, "Comparison of Orthogonal Frequency-Division Multiplexing and Pulse-Amplitude Modulation in Indoor Optical Wireless Links," *IEEE Trans. Commun.*, vol. 60, 2012.
- [15] J. R. Barry, J. M. Kahn, W. J. Krause, E. A. Lee and D. Messerschmitt, "Simulation of multipath impulse response for indoor wireless optical channels," in *IEEE Journal on Selected Areas in Communications*, vol. 11, no. 3, pp. 367-379, April 1993.
- [16] Y. Liu and all, "Waveform Design for 5G Networks: Analysis and Comparison," *IEEE Access*, vol. 5, pp. 19282-19292, 2017.
- [17] C. Kim, K. Kim, Y. H. Yun, Z. Ho, B. Lee and J. Seol, "QAM-FBMC: A New Multi-Carrier System for Post-OFDM Wireless Communications," in *IEEE Global Communications Conference (GLOBECOM)*, San Diego, CA, 2015.
- [18] F. Schaich, T. Wild and Y. Chen, "Waveform Contenders for 5G - Suitability for Short Packet and Low Latency Transmissions," in *IEEE 79th Vehicular Technology Conference (VTC Spring)*, Seoul, 2014.
- [19] B. Farhang-Boroujen and C. Yuen, "Cosine Modulated and Offset QAM Filter Bank Multicarrier Techniques: A Continuous-Time Prospect," *EURASIP Journal on Advances in Signal Processing*, vol. 2010, 2010.
- [20] X. Zhang, M. Jia, L. Chen, J. Ma and J. Qiu, "Networks, Filtered-OFDM - Enabler for Flexible Waveform in The 5th Generation Cellular," in *IEEE Globecom*, San Diego, CA, Dec. 2015.
- [21] X. Zhang, L. Chen, J. Qiu and J. Abdoli, "On the Waveform for 5G," *IEEE Communications Magazine*,

vol. 54, pp. 74-80, 2016.

- [22] Y. Cai, Z. Qin, F. Cui, G. Y. Li and J. A. McCann, "Modulation and Multiple Access for 5G Networks," *IEEE Communications Surveys & Tutorials*, vol. 20, pp. 629-646, 2018.
- [23] A. Ekti, A. Boyaci, A. Alparslan, I. Ünal, S. Yarkan, A. Görçin, H. Arslan and M. Uysal, "Statistical modeling of propagation channels for Terahertz band," in *2017 IEEE Conference on Standards for Communications and Networking (CSCN)*, Helsinki, 2017.
- [24] Wortecs, "D3.1: Gbps wireless radio and Gbps wireless optical communication specifications and evaluations," Oct. 2018.
- [25] F. Lopez-Hernandez, R. Perez-Jimenez and A. Santamaria, "Monte Carlo calculation of impulse response on diffuse IR wireless indoor channels," *Electronics Letter*, vol. 34, no. 12, pp. 1260-1262, 1998.
- [26] A. Behloul, P. Combeau and L. Aveneau, "MCMC Methods for Realistic Indoor Wireless Optical Channels Simulation," *IEEE Journal of Lightwave Technology*, vol. 35, no. 9, 2017.
- [27] K. Miramirkhani, O. Narmanlioglu, M. Uysal and E. Panayirci, "A mobile Channel Model for VLC and Application to Adaptive System Design," *IEEE Communications Letters*, vol. 21, no. 5, 2017.
- [28] WORTECS, "D2.2: WORTECS VR use-cases and requirements," 2018.
- [29] J. Carruthers, S. Carroll and P. Kannan, "Propagation Modeling for Indoor Optical Wireless Communications using fast Multireceiver Channel Estimation," [Online]. Available: <http://citeseerx.ist.psu.edu/viewdoc/download?doi=10.1.1.460.2678&rep=rep1&type=pdf>. [Accessed 10 01 2019].
- [30] S. Priebe, M. Jacod and KürnerT., "Angular and RMS delay spread modeling in view of THz indoor communication systems," *Radio Science*, vol. 49, no. 3, pp. 242-251, 2014.
- [31] "JPL's Wireless Communication Reference Website," [Online]. Available: <http://www.wirelesscommunication.nl/reference/chaptr03/cohbw/cohbw.htm>. [Accessed 25 01 2019].
- [32] ITU, "ITU-R Radiocommunication sector of ITU, Attenuation by atmospheric gases, Recommendation ITU-R P.676-11, 2016."
- [33] S. a. Z. B. a. Z. M. Samadi, "BANDWIDTH OPTIMIZATION TO ACHIEVE MINIMUM PHASE NOISE IN FREQUENCY SYNTHESIZERS," *IRANIAN JOURNAL OF SCIENCE AND TECHNOLOGY-TRANSACTIONS OF ELECTRICAL ENGINEERING*, vol. 38, pp. 21-32, 2014.
- [34] I. Dedic, "56Gs/s ADC : Enabling 100GbE," in *2010 Conference on Optical Fiber Communication (OFC/NFOEC), collocated National Fiber Optic Engineers Conference*, San Diego, CA, USA, 2010.
- [35] M. S. K. K. M. E. M. Mohankumar, "Fpga Implementation of Mimo-Ofdm for Baseband Modem Parallel Architecture," *INTERNATIONAL JOURNAL OF ENGINEERING RESEARCH & TECHNOLOGY (IJERT)*, vol. 02, no. 03, 2013.
- [36] E. Satorius, "Parallel Modem Architectures for High-Data-Rate Space Modems," *Interplanetary Network Progress Report*, vol. 198, pp. 1-11, 2014.
- [37] B. T. a. S. S. a. M. Rupp, "BER comparison between Convolutional, Turbo, LDPC, and Polar codes," in *24th International Conference on Telecommunications (ICT)*, Limassol, Cyprus, 2017.
- [38] J. Z. a. R. Chen, "Achieving Transmit Diversity in OFDM-IM by Utilizing Multiple Signal Constellations," *IEEE Access*, vol. 5, pp. 8978 - 8988, 2017.
- [39] M. E. a. M. Petri, "60 GHz wireless broadband cable replacement for machine vision applications," in *International Symposium on Signals, Systems, and Electronics (ISSSE)*, Potsdam, Germany, 2012.
- [40] E. S. a. H. E.-G. a. D. McNeill, "Frequency offset estimation and correction in the IEEE 802.11a WLAN," in *IEEE 60th Vehicular Technology Conference, 2004. VTC2004-Fall. 2004*, Los Angeles, CA, USA, 2004.
- [41] G. Berhault, C. Leroux, C. Jego and D. Dallet, "Partial sums generation architecture for successive," *Signal Processing Systems (SiPS)*, pp. 407-412, Oct. 2013.
- [42] ITU, "G.9960 : Unified High-speed wireline-based home networking transceivers -System architecture and physical layre specification," [Online]. Available: <https://eee.itu.int/rec/T-REC-G.9960-201811-I/en>.